

~~CONFIDENTIAL~~

NASA MEMO 2-2-59A

NASA

## MEMORANDUM

PERFORMANCE OF A TOP INLET WITH A VERTICAL POROUS  
WEDGE AT MACH NUMBERS OF 1.6 TO 2.35

By A. Vernon Gnos

Ames Research Center  
Moffett Field, Calif.

CLASSIFICATION CHANGED TO UNCLASSIFIED  
BY AUTHORITY OF NASA CLASSIFICATION CHANGE  
NOTICES. CHANGE NO. 109-16. EFF. 10/19/70  
*ju*

CLASSIFIED DOCUMENT - TITLE UNCLASSIFIED

This material contains information affecting the National Defense of the United States within the meaning of the espionage laws, Title 18, U.S.C., Secs. 793 and 794, the transmission or revelation of which in any manner to an unauthorized person is prohibited by law.

NATIONAL AERONAUTICS AND  
SPACE ADMINISTRATION

WASHINGTON

May 1959

~~CONFIDENTIAL~~

UNCLASSIFIED

16754

UNCLASSIFIED

NATIONAL AERONAUTICS AND SPACE ADMINISTRATION

MEMORANDUM 2-2-59A

PERFORMANCE OF A TOP INLET WITH A VERTICAL POROUS

WEDGE AT MACH NUMBERS OF 1.6 TO 2.35\*

By A. Vernon Gnos

SUMMARY

An experimental investigation has been conducted to determine the performance of a three-shock external-compression variable-geometry inlet located behind a cockpit enclosure on the top of the fuselage of a proposed airplane configuration. Compression of the air was achieved by a vertical wedge centrally mounted in the inlet and having a fixed-angle first ramp and a variable-angle second ramp. Performance effects of wedge boundary-layer removal with two compression surface porosities and two bleed exit areas at the top of the duct were determined. The effects of variable second wedge angle, angle-of-attack characteristics, and performance at angles of sideslip with symmetric and asymmetric wedge deflection were also investigated. The ranges of Mach number, angle of attack, and angle of sideslip were 1.6 to 2.35,  $-6^{\circ}$  to  $20^{\circ}$ , and  $-9^{\circ}$  to  $4^{\circ}$ , respectively.

With wedge boundary-layer bleed, pressure recoveries of 0.93 and 0.89 were obtained at Mach numbers 1.6 and 2.0. Distortion was significantly decreased as a result of bleed. At engine matched mass flow, bleed increased effective thrust ratio by 3 and 13 percent at Mach numbers 1.6 and 2.0.

Wedge-angle variations up to  $\pm 3^{\circ}$  from the optimum setting at Mach number 1.6 or about  $\pm 2^{\circ}$  at Mach number 2.0 caused a loss in pressure recovery of less than 1 percent.

Pressure recovery was maintained up to  $15^{\circ}$  angle of attack at Mach number 1.6 and  $7^{\circ}$  at Mach number 2.0. The stable range of mass flow was maintained nearly constant up to  $12^{\circ}$  angle of attack.

Asymmetric second-wedge deflections of  $1^{\circ}$  per degree of sideslip were effective in maintaining pressure recovery and delaying buzz at engine matched mass flow.

\*Title, Unclassified.

UNCLASSIFIED

## INTRODUCTION

A top inlet location offers several advantages over other inlet positions. Some of these advantages are: store carrying capacity can be greater, stores can be carried internally or semisubmerged, and ingestion of foreign objects from runways is less likely to occur. Angle-of-attack performance of top inlet configurations is, however, adversely affected by body crossflow and boundary-layer thickening. It is therefore difficult to determine a satisfactory fuselage forebody shape in combination with a top inlet location which will provide high performance at angles of attack. Further, compression surfaces should be incorporated which are insensitive to angle of attack. The investigations of references 1 and 2 have indicated that vertical-wedge compression surfaces are satisfactory from this latter standpoint.

For the present investigation a vertical-wedge inlet was located on top of the fuselage of a complete model configuration of a fighter-bomber-type airplane. This was the same model that was used in the investigation of reference 3. The test had as its objectives the determination of the effects of compression surface boundary-layer bleed upon pressure recovery and distortion, the drag penalty associated with discharging bleed air, the effects of variable-wedge angle upon inlet performance, and the optimum wedge angle for each Mach number. Angle-of-attack characteristics and performance at angles of sideslip with symmetric and asymmetric wedge deflection were also investigated.

The tests were performed in the 9- by 7-foot test section of the Ames Unitary Plan supersonic wind tunnel at Mach numbers of 1.6 to 2.35. Reynolds number was approximately 2.5 million per foot.

## SYMBOLS

$A_1$	capture area, 0.054 sq ft
$A_3$	duct area at compressor face, 0.057 sq ft
$C_D$	drag coefficient referred to stability axes, $\frac{D}{qS}$
$D$	drag, lb
$F_n$	engine net thrust, lb
$\frac{F_n - D}{F_{n_i}}$	effective-thrust ratio

A-141

M	Mach number
m	mass flow, slugs/sec
$\frac{m_w}{m_\infty}$	wedge boundary-layer-bleed mass-flow ratio
$\frac{m_3}{m_\infty}$	mass-flow ratio, $\frac{\text{compressor mass flow}}{\text{free-stream mass flow based on capture area}}$
$\frac{m_2}{m_\infty}$	inlet mass-flow ratio, $\frac{m_3}{m_\infty} + \frac{m_w}{m_\infty}$
$\Delta p$	compressor-face total-pressure distortion, $\frac{(p_{t3})_{\max} - (p_{t3})_{\min}}{p_{t3}}$
$p_t$	total pressure, lb/sq ft
$\frac{p_{t3}}{p_{t\infty}}$	pressure recovery
q	dynamic pressure, lb/sq ft
S	wing area, 3.046 sq ft
w	engine air-flow rate, lb/sec
$\frac{w\sqrt{\theta}}{\delta A_3}$	corrected air-flow rate, lb/sec/sq ft
$\alpha$	angle of attack, deg
$\beta$	angle of sideslip, deg
$\delta$	compressor-face total pressure divided by standard sea-level pressure
$\theta$	compressor-face total temperature divided by standard sea-level temperature
$\sigma$	wedge half-angle of second ramp with respect to fuselage center line, deg
$\Delta\sigma$	change of wedge half-angle from symmetric position, positive direction to the left, deg

## Subscripts

1	capture station
2	inlet station
3	compressor-face station
$\infty$	free-stream condition
i	ideal
L	left
R	right
w	wedge

## Bleed Configurations

$P_5$	5-percent-open, variable-wedge, porous plate and inner diffuser wall porous plate
$P_{15}$	15-percent-open, variable-wedge, porous plate and 3-percent-open, inner diffuser wall porous plate
$E_0$	closed porous-wedge bleed exit
$E_S$	small porous-wedge bleed exit, 0.0089 sq ft
$E_L$	large porous-wedge bleed exit, 0.0112 sq ft

## MODEL AND TESTS

## Model Description

Illustrations of the test model are shown in the photographs of figure 1 and the sketches of figures 2 and 3. The inlet, located above and behind the canopy as shown in figure 2, was split into two ducts by a vertical wedge. The two ducts rejoined to form a single diffuser just upstream of the compressor-face station. External compression was accomplished by two oblique shock waves, the first from a fixed wedge with a  $6^\circ$  half-angle and the second from a variable wedge. The variable-wedge

angle limits of  $3-1/4^\circ$  and  $19^\circ$  are indicated in figure 3(a). Compression surface bleed was applied through the porous surface of the variable wedge and the inner diffuser wall. The inlet was designed to operate with the first oblique shock on the outer lip at about Mach number 2.1. A fuselage boundary-layer splitter plate which formed the floor of the inlet (illustrated in figs. 1 and 3(a)) was cut back in conformance with the results of reference 2. Asymmetric wedge deflection is shown in figure 3(b). Subsonic diffuser area measured normal to the flow is presented in figure 4.

The extent of porous surfaces on the variable wedge and the inner diffuser wall is shown in figures 2 and 3. The porous surfaces were formed of smooth plates with uniformly spaced circular holes normal to the surface. Two configurations of porosity were tested: (1) 5-percent-open plates on both surfaces, and (2) a 15-percent-open plate on the variable wedge and a 3-percent-open plate on the inner diffuser wall.

A cavity behind the variable wedges and inner diffuser walls served as a plenum chamber for compression surface boundary-layer bleed air. The air was then discharged through a flush exit located above the wedge chamber. Details of the exit are shown in figures 1(c) and 2. Three exit configurations were tested: (1) closed, (2) a small exit with a combined exit area of 0.0089 square feet, and (3) a large exit with a total exit area of 0.0112 square feet, as shown in figure 1(c).

The test model was mounted on a 7-component strain-gage balance held by a hollow sting so that forces and moments were recorded simultaneously with the internal-flow measurements. The balance, consisting of 4 normal-force gages, 2 side-force gages, and a chord-force gage was built around the duct. Mass flow was controlled with an iris valve located at the exit of the offset support sting.

### Instrumentation

Compressor-face instrumentation at air-flow station 3 consisted of 36 total-pressure and 12 static-pressure tubes. The total-pressure tubes were arranged in 6 rakes, each with 6 tubes spaced to enable area-weighted total-pressure integration. Six of the static-pressure tubes were placed in the wall of the duct and the other 6 were in the surface of the compressor hub.

A flow meter, built into the hollow support sting and located about 57 inches downstream of the compressor face, was used to measure mass flow. Special care was taken to insure accurate measurement of mass flow.

A single static-pressure tube was located in the wedge chamber.

Total drag was measured with an internal strain-gage balance built into the model around the duct. Duct labyrinth seal leakage air which exited at the base of the model necessitated extensive base-pressure instrumentation. Base pressure was measured as the average of 11 static-pressure tubes, 6 located on the sting at the base of the model and 5 located in the chamber between the sting and the model shell.

In order to determine exit momentum of the internal flow, duct exit static pressure was measured as the average reading of 4 tubes located at about station 52.

A pressure transducer located in the floor of the duct immediately downstream of the vertical-wedge assembly was used to detect "buzz" (defined as unsteady flow in the inlet and subsonic diffuser at subcritical mass-flow conditions).

### Test Procedure

The tests were conducted at free-stream Mach numbers of 1.6, 1.8, 2.0, 2.1, 2.2, and 2.35. The angles of attack and sideslip were varied from  $-6^\circ$  to  $20^\circ$  and from  $-9^\circ$  to  $4^\circ$ , respectively. Wedge half-angles were varied from  $3-1/4^\circ$  to  $19^\circ$ . The range of ratios of asymmetric wedge deflection to sideslip angle ( $\Delta\sigma/\beta$ ) was from 0 to 3.0.

### Data Reduction

Data were reduced to standard coefficient and dimensionless ratio form. Drag corrections were made for base pressure variations and for buoyancy which is a result of tunnel longitudinal static-pressure variation.

Internal drag, which in this investigation was considered to be the change in momentum from the free stream to duct exit of the air passing the compressor station, was subtracted from measured drag. Duct exit momentum was calculated from the measured exit static pressure by use of one-dimensional flow equations. Correcting measured model attitudes for tunnel stream angle and for sting and balance load deflections determined angles of attack and sideslip.

In order that the mass flow through the bleed exit could be calculated, the following assumptions were made: (1) flow was choked at the exit or the bleed exit static pressure was equal to free-stream static pressure, depending on wedge chamber pressure; (2) the flow velocity

within the wedge plenum chamber was low enough that total pressure was indicated by the static-pressure tube; and (3) one tube gave the average pressure of the entire chamber.

## RESULTS AND DISCUSSION

The results of this investigation are discussed in the following sequence: first, the effects of bleed area and the best bleed configuration; second, with the best bleed configuration, the effects of wedge-angle variation; third, inlet performance over the angle-of-attack range; fourth, inlet performance over the range of angles of sideslip with symmetric and asymmetric wedge angles.

### Bleed Effects

Several combinations of bleed exit area and wedge porosity were used to determine the effectiveness of compression surface boundary-layer bleed. The results are presented in figures 5 and 6. (See SYMBOLS for configuration designations.)

In figure 5 inlet characteristics are presented as a function of inlet mass flow. Application of bleed increased the pressure recovery, increased the drag coefficient, and decreased distortion substantially. The various combinations of exit area and porosity all exhibited about the same improvement in pressure recovery and decrease in distortion compared to the closed bleed exit configuration. Therefore only one configuration,  $P_{15}E_7$ , was used for the remainder of the test. Wedge bleed mass flow, and correspondingly drag, increased both with increase in variable-wedge porosity and exit area.

A comparison of pertinent performance characteristics with and without bleed ( $P_{15}E_7$  and  $P_5E_0$ , respectively) at an angle of attack of  $2^\circ$  near critical inlet mass-flow ratios is summarized as follows:

$M_\infty$	$\sigma$ , deg	$\frac{m_2}{m_\infty}$	$p_{t3}/p_{t\infty}$		$C_D$		$\Delta p$		$p_{t3}/p_{t\infty}$ increase, percent	$C_D$ increase, percent
			No bleed	Bleed	No bleed	Bleed	No bleed	Bleed		
1.6	9	0.82	0.90	0.95	0.0380	0.0404	0.19	0.07	5.6	6.3
1.8	12	.85	.85	.91	.0370	.0394	.22	.07	7.1	6.5
2.0	17	.85	.79	.90	.0364	.0390	.21	.06	13.9	7.1



The closed bleed exit configuration ( $P_5E_0$ ) retained the 5-percent porous plates on the wedge and inner diffuser wall. As a result, recirculation occurred through the porous plates with unknown effects on pressure recovery and distortion.

Examination of the table reveals that the gain in pressure recovery as a result of boundary-layer bleed increased with Mach number while the drag penalty associated with discharging the bleed air remained nearly constant. Performance improvement with bleed became significant only above a Mach number of 1.8 inasmuch as the increases in drag and pressure recovery nearly offset each other at Mach numbers of 1.6 and 1.8. Bleed significantly reduced the total-pressure distortion at all Mach numbers.

In figure 6 typical inlet characteristics are presented as a function of compressor mass flow in order to evaluate the inlet performance when matched with a specific engine. Air-flow requirements, which comprise compressor-air requirements plus cooling air, and thrust characteristics were assumed for a conventional two-spool turbojet engine with afterburner. The conditions for engine matching were a standard day and an altitude of 35,000 feet.

Application of bleed increased the pressure recovery from 2 to 9 percent and effective-thrust ratio from 3 to 13 percent of ideal net thrust but had little effect on stable range of mass flow. A comparison of the performance characteristics with and without bleed ( $P_{15}E_7$  and  $P_5E_0$ , respectively) at  $2^\circ$  angle of attack at engine matched mass-flow ratio is summarized below:

$M_\infty$	$\sigma$ , deg	$P_{t3}/P_{t\infty}$		$C_D$		$F_{n-D}/F_{n1}$		$P_{t3}/P_{t\infty}$	$C_D$	$F_{n-D}/F_{n1}$
		No bleed	Bleed	No bleed	Bleed	No bleed	Bleed	increase, percent	increase, percent	increase
1.6	9	0.91	0.93	0.0391	0.0392	0.16	0.19	2.2	0	0.03
1.8	12	.86	.91	.0384	.0385	.01	.08	5.8	0	.07
2.0	17	.82	.89	.0390	.0372	-.18	-.05	8.5	-4.6	.13

Application of bleed gave a large increase in effective thrust ratio at a Mach number of 2.0 and lesser increases at the lower Mach numbers.<sup>1</sup> At a Mach number of 2.0, the stable operating range of mass flow with bleed was about 16.2 percent of the maximum mass-flow ratio. Changes in bleed exit area or wedge porosity had little effect on the stable range.

<sup>1</sup>Drag of the configuration without bleed ( $P_5E_0$ ) was not adjusted to account for the inlet effectively being too large since it was assumed that this would result in only a small difference in the comparison of thrust ratio.

A significant effect of bleed was the decrease in distortion as shown in figure 7. Contours of local total-pressure recovery are compared near critical inlet mass-flow ratio. Bleed improved pressure distribution as a result of an increase in total pressure at the bottom of the duct. The high-pressure regions on either side of the compressor hub are similar to, but less severe than, those found in the underslung inlet of reference 2.

### Wedge-Angle Effects

Characteristics of the inlet for second wedge angles from  $3\text{-}1/4^\circ$  to  $19^\circ$  with bleed applied ( $P_{15}E_1$ ) are shown in figure 8. The results of performance at engine matched mass flow are summarized in figure 9. Wedge angle may be varied from the optimum setting by about  $\pm 3^\circ$  at a Mach number of 1.6 or about  $\pm 2^\circ$  at a Mach number of 2.0 with a drop in pressure recovery of less than 1 percent. The thrust ratio curves are similarly flat in the region near their maximum values. Therefore, a coarse setting of wedge angle is allowable with little sacrifice in performance. The second wedge angles for maximum net thrust, as indicated in figure 9, are  $9^\circ$ ,  $13^\circ$ , and  $17^\circ$  at Mach numbers of 1.6, 1.8, and 2.0, respectively. With these wedge angles, the stable operating range decreased from 24 percent of maximum mass-flow ratio at Mach number 1.6 to 16 percent at Mach number 2.0.

### Characteristics at Angle of Attack

Figure 10 indicates the performance characteristics of the inlet with bleed ( $P_{15}E_1$ ) at various angles of attack. Pressure recovery and distortion generally were little affected by angle of attack. Stable operating range was about constant for angles of attack between  $2^\circ$  and  $12^\circ$ . The good pressure-recovery performance of the inlet at angles of attack indicates that the fuselage crossflow had minor effects.

Figure 11 indicates inlet pressure-recovery and distortion characteristics near engine matched mass flow. Angle-of-attack effects for the bleed configuration ( $P_{15}E_1$ ) are shown. Pressure recovery was maintained up to  $15^\circ$  angle of attack at Mach number 1.6 and  $7^\circ$  at Mach number 2.0.

The compressor-face pressure-recovery contours of figure 12 illustrate the effects of angle of attack near engine matched mass flow. Figure 7 may be referred to for additional comparisons.

## Characteristics at Angle of Sideslip

Symmetric wedge deflections.- Figure 13 presents the performance of the top inlet at angles of sideslip. Wedge deflection was symmetric; that is, the left and right wedge angles were equal. The data were taken at  $2^\circ$  angle of attack except where flagged symbols indicate  $0^\circ$  angle of attack. Pressure recovery and distortion were not affected by these differences in angle of attack; the drag however was adjusted. The loss in pressure recovery and increase in distortion with sideslip angle was large. Most important was the buzz which occurred at small angles of sideslip. In addition, the stable operating range decreased with sideslip angle. As a result, there was heavy buzz at the engine match point in many instances. An undesirable characteristic of this inlet fuselage combination in sideslip attitudes is indicated in reference 3. With symmetric wedge deflection and reduced mass flow (buzz present) the model experienced large changes in directional stability near  $0^\circ$  sideslip. This was the result of twin-duct instability (ref. 4) at very low mass-flow ratios.

Asymmetric wedge deflections.- As a method to overcome the difficulties at angles of sideslip, asymmetric wedge deflection was investigated. The method and direction of wedge deflection is illustrated in figure 3(b). Windward wedge deflection was reduced and leeward wedge deflection was increased as sideslip angle was increased. Inlet performance with asymmetric wedge deflection is presented in figure 14. Asymmetric wedge deflection was effective in extending the stable range of mass flow, increasing pressure recovery, and decreasing distortion during sideslip. A match point in the stable operating range of mass flow was always possible by proper selection of asymmetric wedge deflection. As previously mentioned, a buzz-free match point was not always possible with symmetric wedge deflection.

A comparison of symmetric and asymmetric wedge inlet performance at engine matched mass flow is shown in figure 15. Performance with various ratios of asymmetric wedge deflection to sideslip angle,  $\Delta\sigma/\beta$ , is presented as a function of sideslip angle. The optimum inlet performance in sideslip was obtained with a ratio of  $\Delta\sigma/\beta$  of 1. For simplicity of control systems, it is desirable to be able to pick a single ratio of  $\Delta\sigma/\beta$  for all sideslip conditions. Asymmetric wedge deflection with this optimum ratio gave highest pressure recovery and least distortion, and permitted a buzz-free engine match point. Performance improvements appeared to increase with Mach number.

The pressure contours of figure 16, when compared with bleed configuration contours of figure 7, disclose the effects of sideslip with symmetric wedge deflection and the improvements obtained with asymmetric wedge deflection. A significant improvement both in pressure recovery on the leeward side of the duct and in distortion is evident when asymmetric wedge deflection is employed.

## SUMMARY OF RESULTS


The performance of a three-shock, external-compression, variable-geometry inlet located behind a cockpit enclosure on the top of a fuselage was determined. The Mach number, angle-of-attack, and angle-of-sideslip ranges of the test were 1.6 to 2.35,  $-6^{\circ}$  to  $20^{\circ}$ , and  $-9^{\circ}$  to  $4^{\circ}$ , respectively. The data indicate:

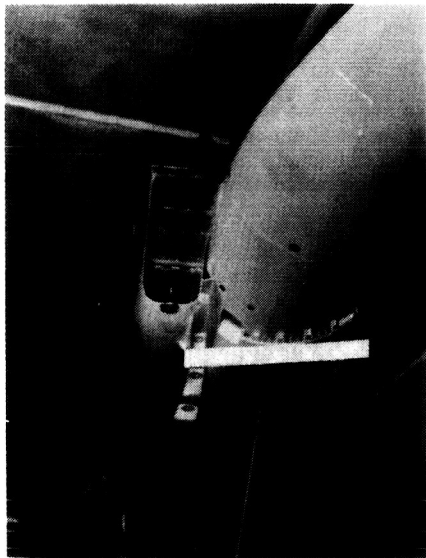
1. With wedge boundary-layer bleed, pressure recoveries of 0.93 and 0.89 were obtained at Mach numbers 1.6 and 2.0. Distortion was significantly decreased as a result of bleed. At engine matched mass flow, bleed increased effective-thrust ratio by 3 and 13 percent at Mach numbers 1.6 to 2.0.
2. Wedge angle variations up to  $\pm 3^{\circ}$  from the optimum setting at Mach number 1.6 or about  $\pm 2^{\circ}$  at Mach number 2.0 caused a loss in pressure recovery of less than 1 percent.
3. Pressure recovery was maintained up to  $15^{\circ}$  angle of attack at Mach number 1.6 and  $7^{\circ}$  at Mach number 2.0. The stable range of mass flow was maintained nearly constant up to  $12^{\circ}$  angle of attack at the Mach numbers tested.
4. Through asymmetric second wedge deflection the undesirable sideslip characteristics of the inlet were overcome. Optimum inlet performance in sideslip was obtained with  $1^{\circ}$  of asymmetric second wedge deflection per degree of sideslip.

Ames Research Center  
National Aeronautics and Space Administration  
Moffett Field, Calif., Nov. 4, 1958

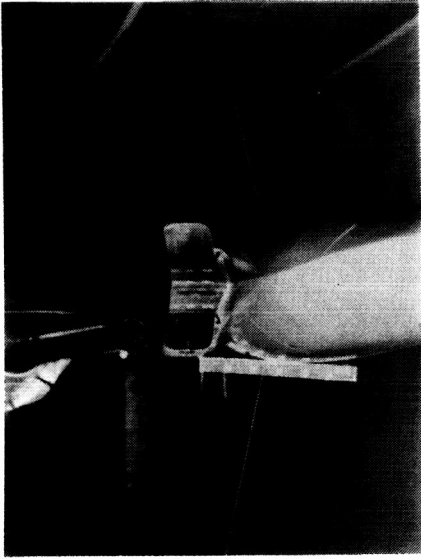
## REFERENCES

1. Leissler, L. Abbot, and Hearsh, Donald P.: Preliminary Investigation of Effect of Angle of Attack on Pressure Recovery and Stability Characteristics for a Vertical-Wedge-Nose Inlet at Mach Number of 1.90. NACA RM E52E14, 1952.
2. Allen, John L., and Piercy, Thomas G.: Performance Characteristics of an Underslung Vertical-Wedge Inlet With Porous Suction at Mach Numbers of 0.63 and 1.5 to 2.0. NACA RM E56B15, 1956.

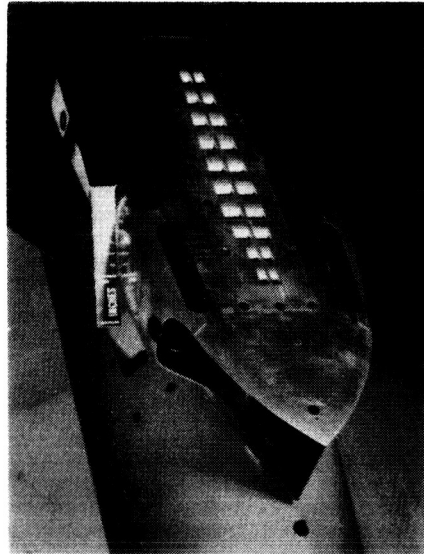
- 
3. Gnos, A. Vernon, and Kurkowski, Richard L.: Static Longitudinal and Lateral Stability and Control Characteristics of a Model of a Swept-Wing Fighter-Bomber-Type Airplane With a Top Inlet at Mach Numbers From 1.6 to 2.35. NACA RM A57K20, 1958.
  4. Beke, Andrew: Criteria for Initial Flow Reversal in Symmetrical Twin-Intake Air-Induction Systems Operating at Supersonic Speeds. NACA RM E55L02a, 1956.



(a) Three-quarter side view; 5-percent open porous plates, closed bleed exit ( $P_5E_0$ ).



(b) Front view; 5-percent open porous plates, closed bleed exit ( $P_5E_0$ ).



(c) Top view, large bleed exit ( $P_5E_7$ ).

Figure 1.- Photographs of inlet.

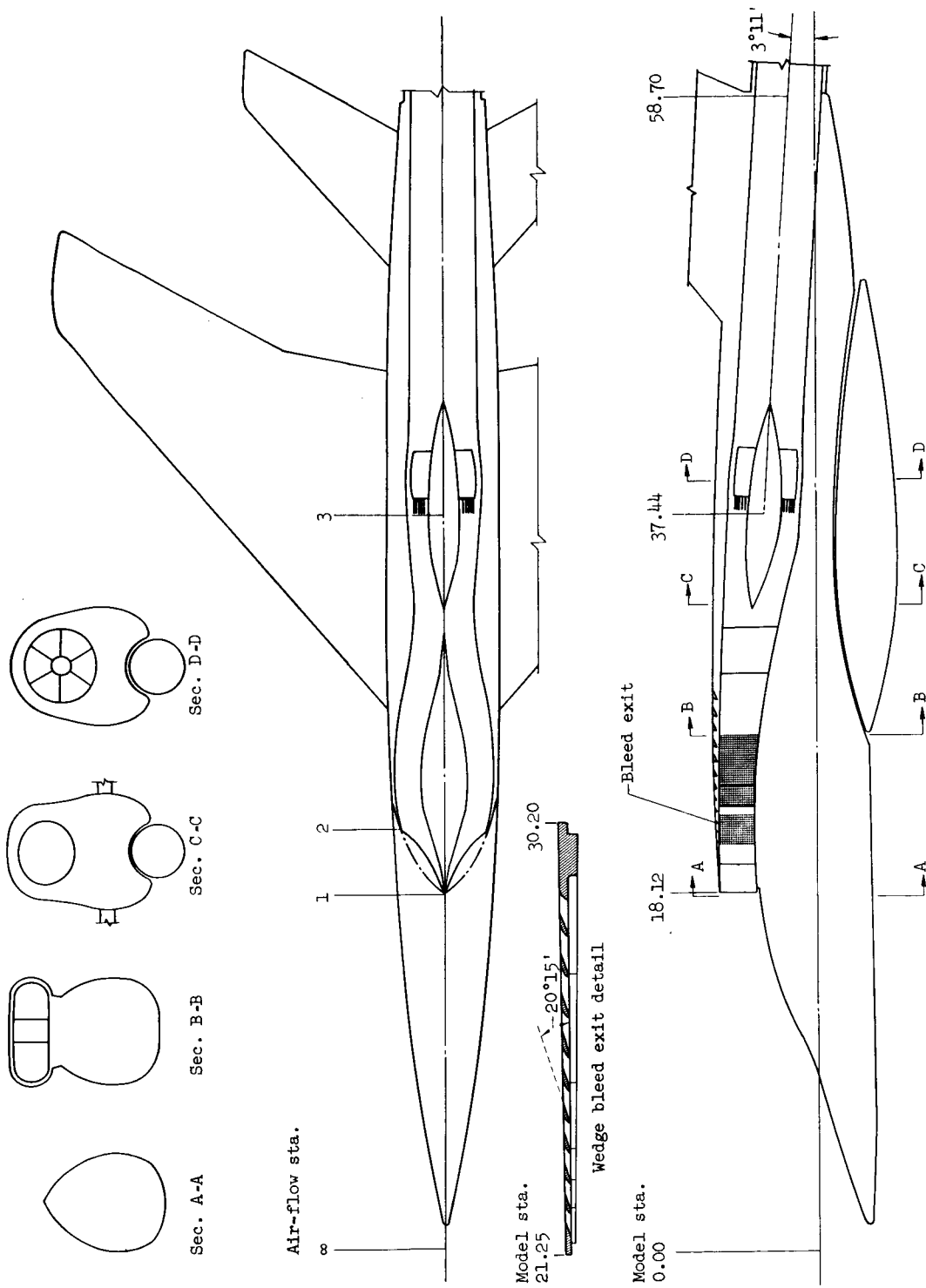
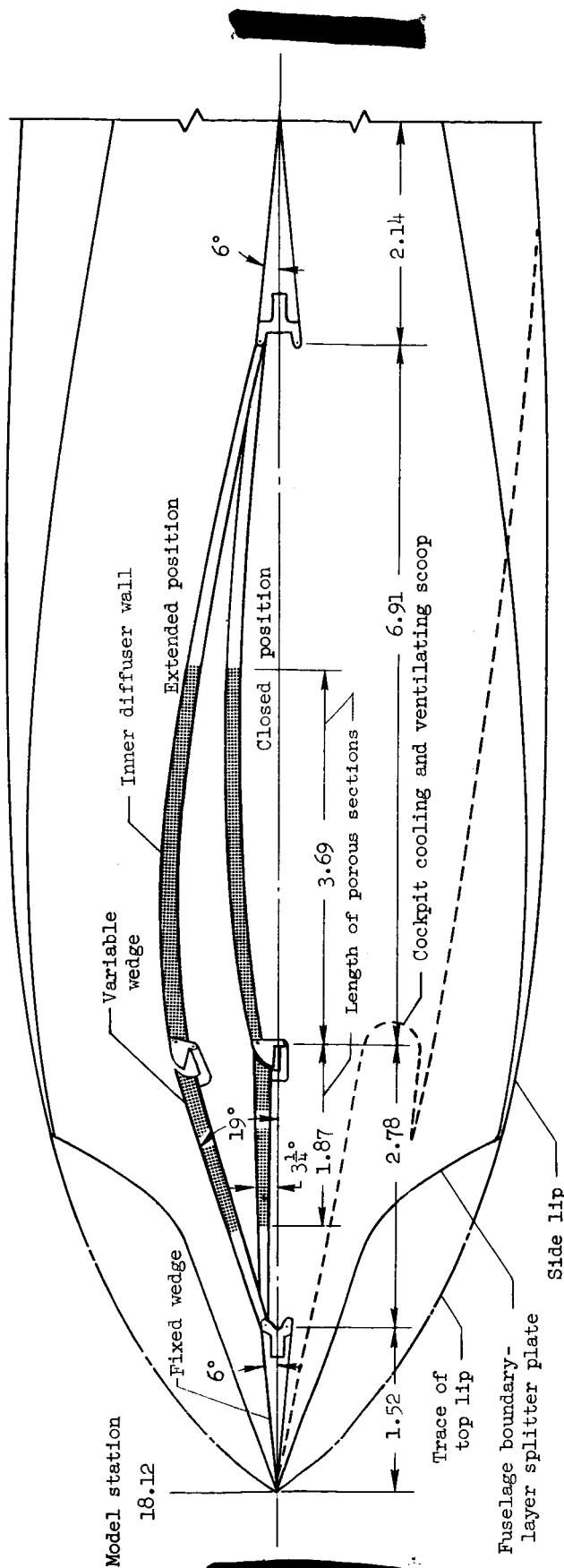


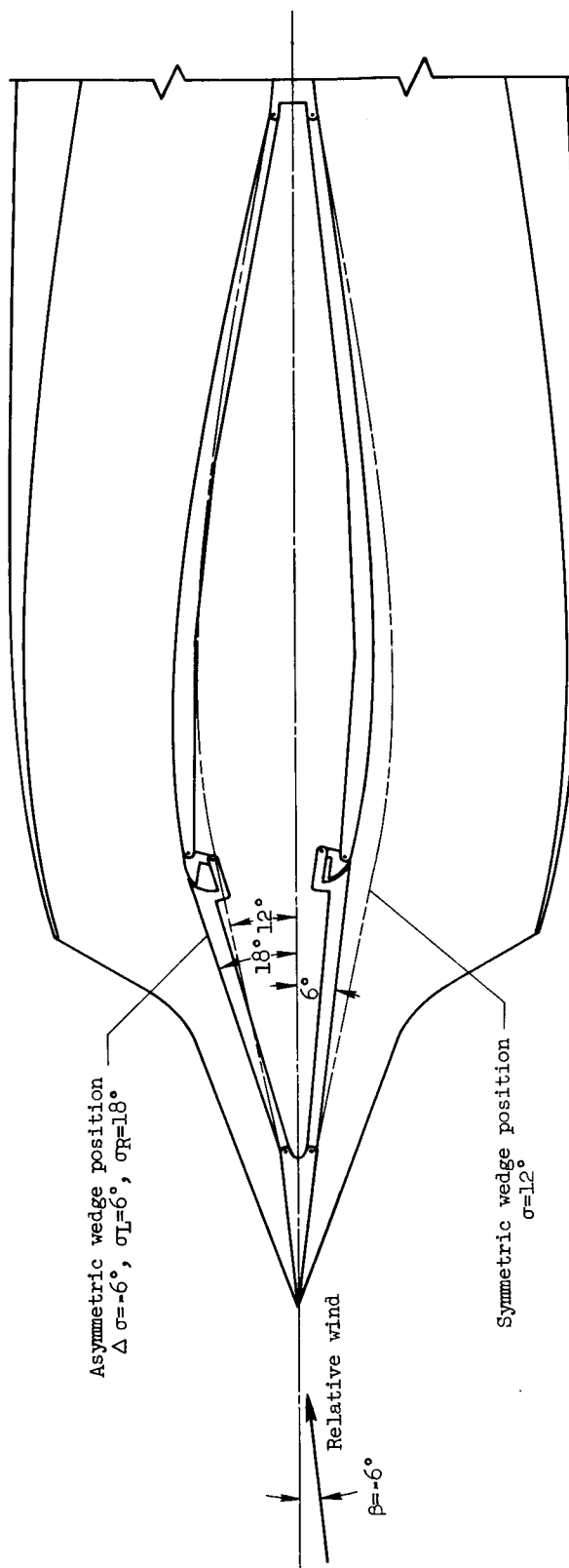
Figure 2.- General arrangement of model.



(a) Detail of wedges, bleed surfaces, fuselage boundary-layer diverter, and inlet lips.

Figure 3.- Inlet detail.





(b) Asymmetric wedge deflection.

Figure 3.- Concluded.

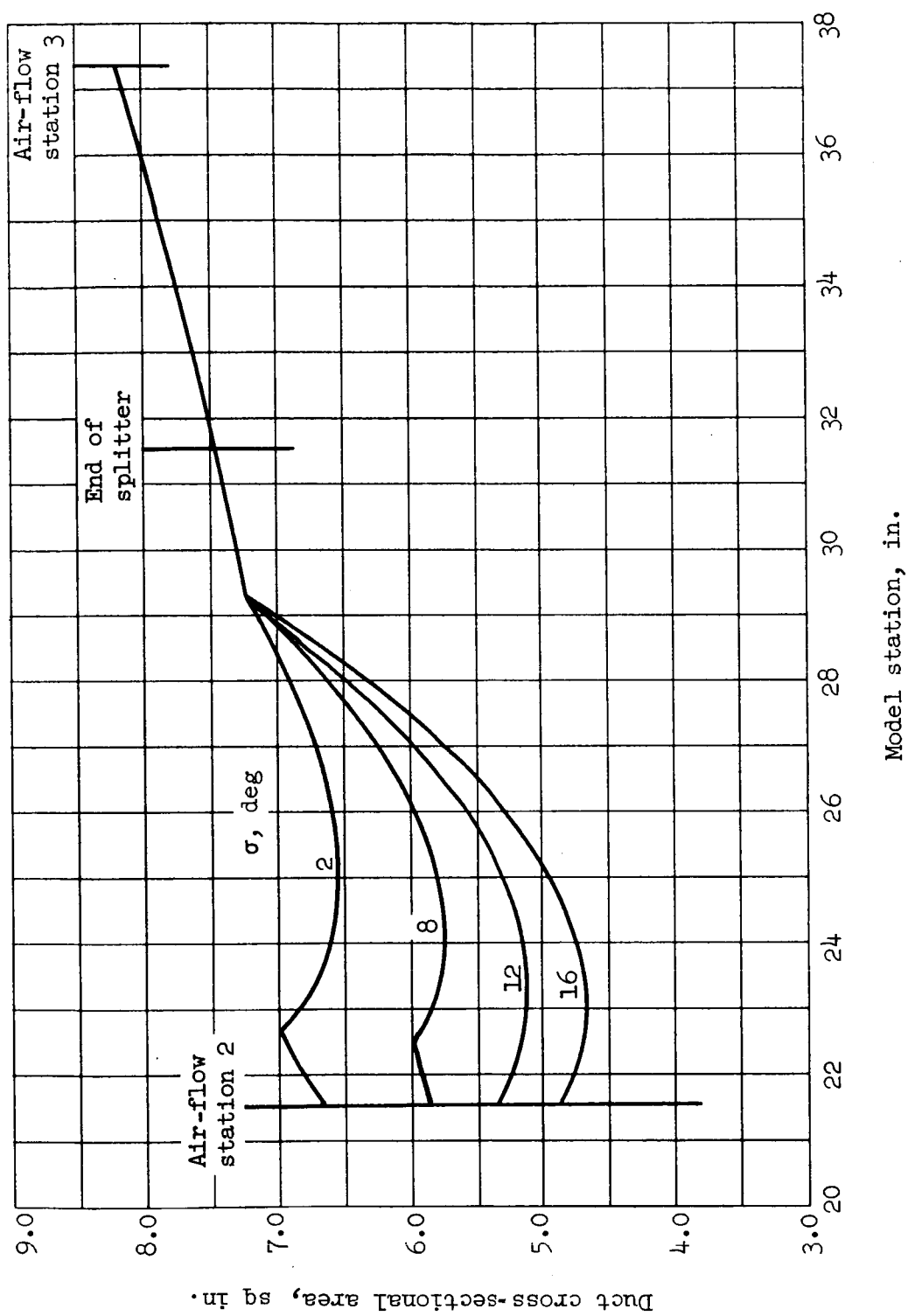


Figure 4.- Subsonic diffuser area variation with symmetric wedge deflection.

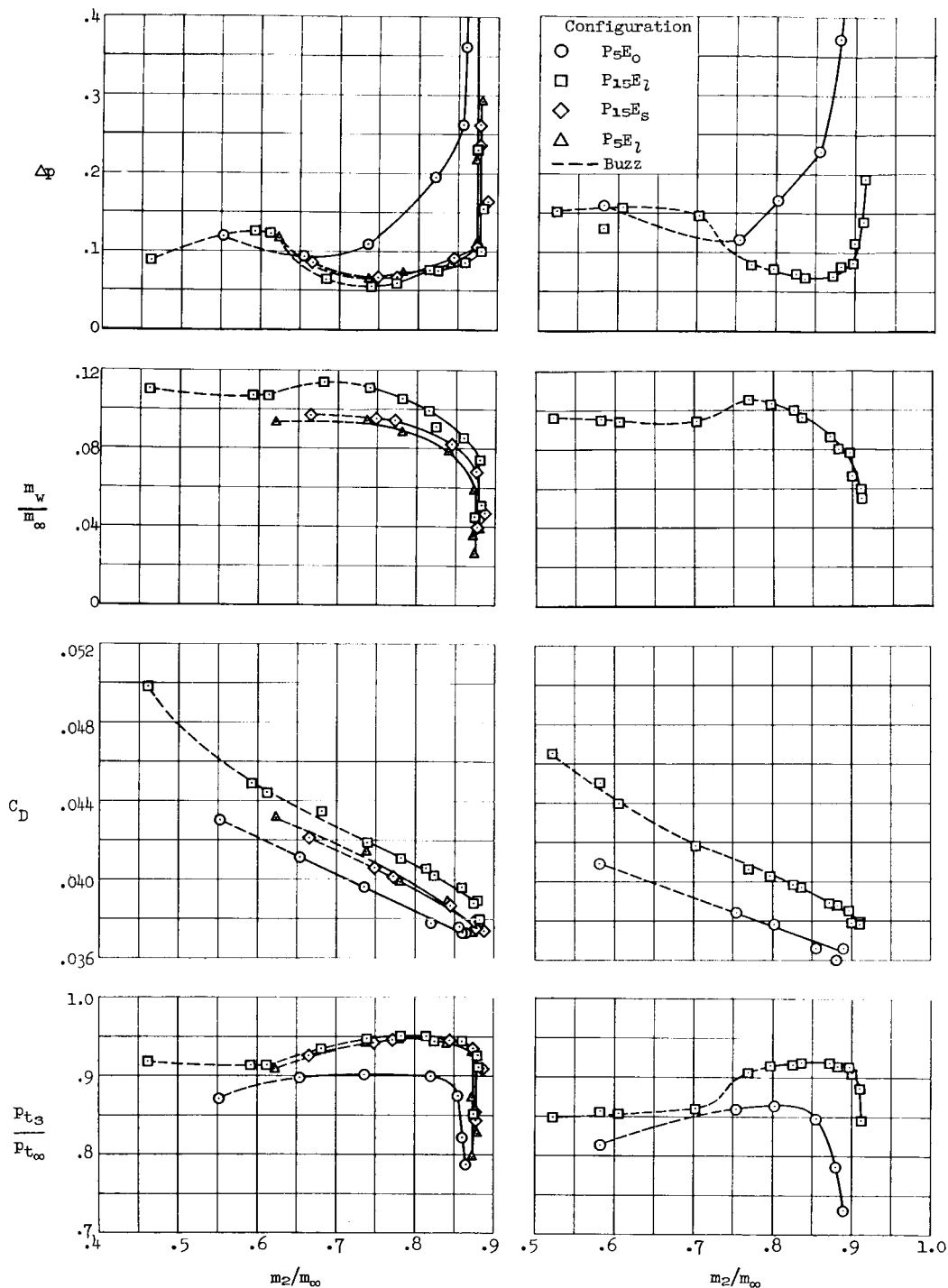


Figure 5.- Comparison of performance of various bleed configurations as a function of inlet mass flow;  $2^\circ$  angle of attack.

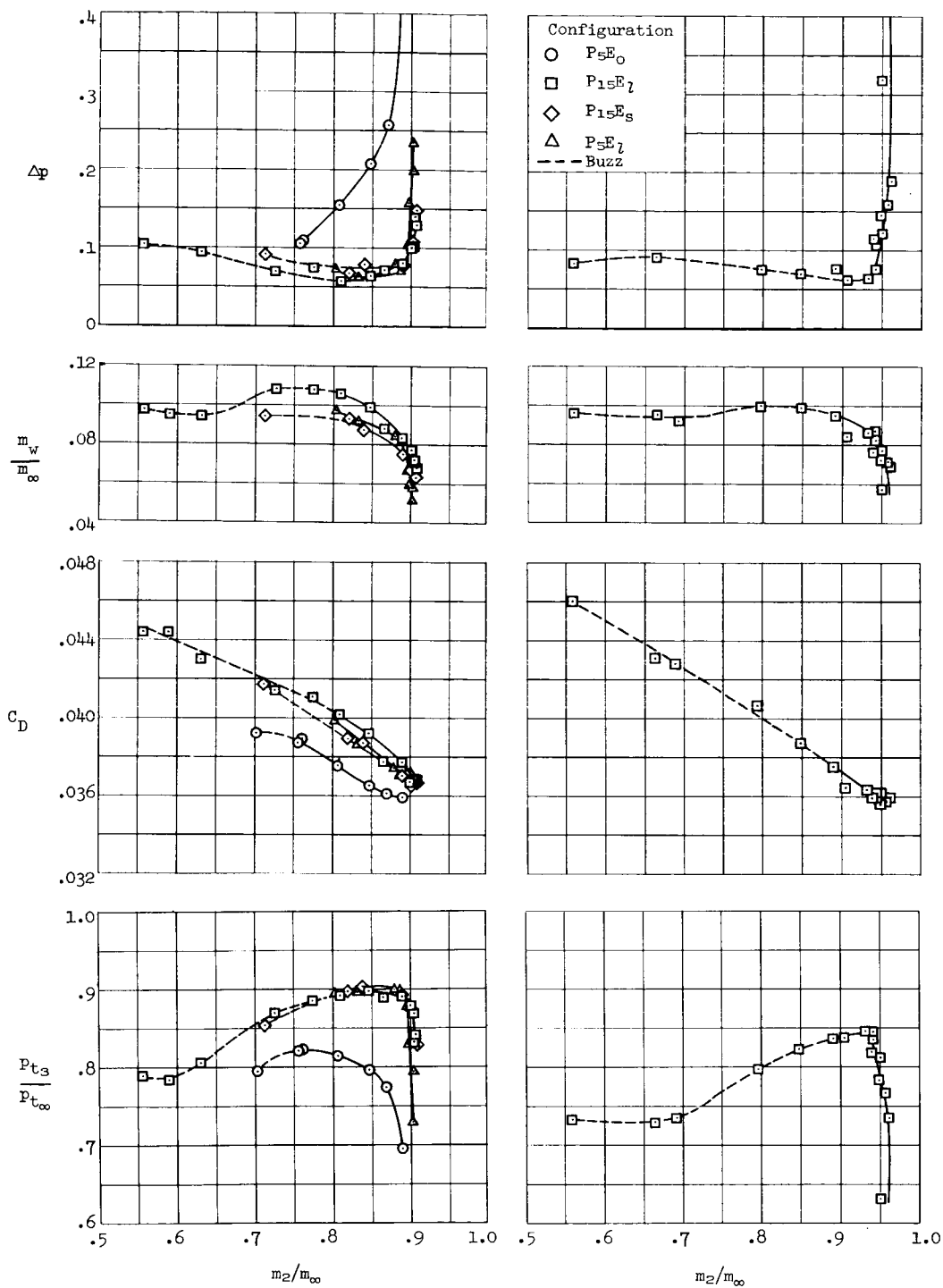
(c)  $M_{\infty}=2.0, \sigma=17^\circ$ (d)  $M_{\infty}=2.2, \sigma=19^\circ$ 

Figure 5.- Concluded.

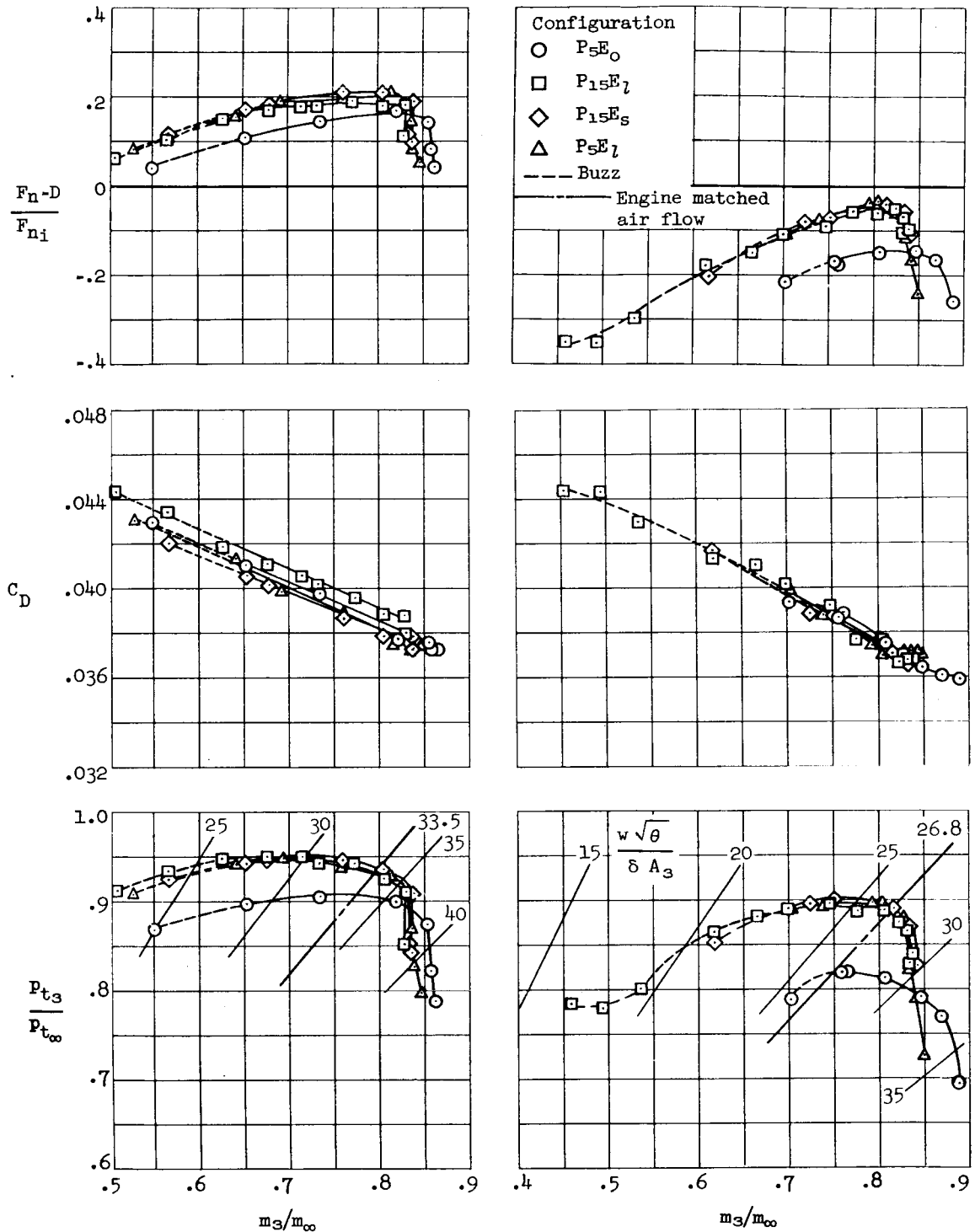


Figure 6.- Comparison of performance of various bleed configurations as a function of compressor mass flow;  $\alpha=2^\circ$ .

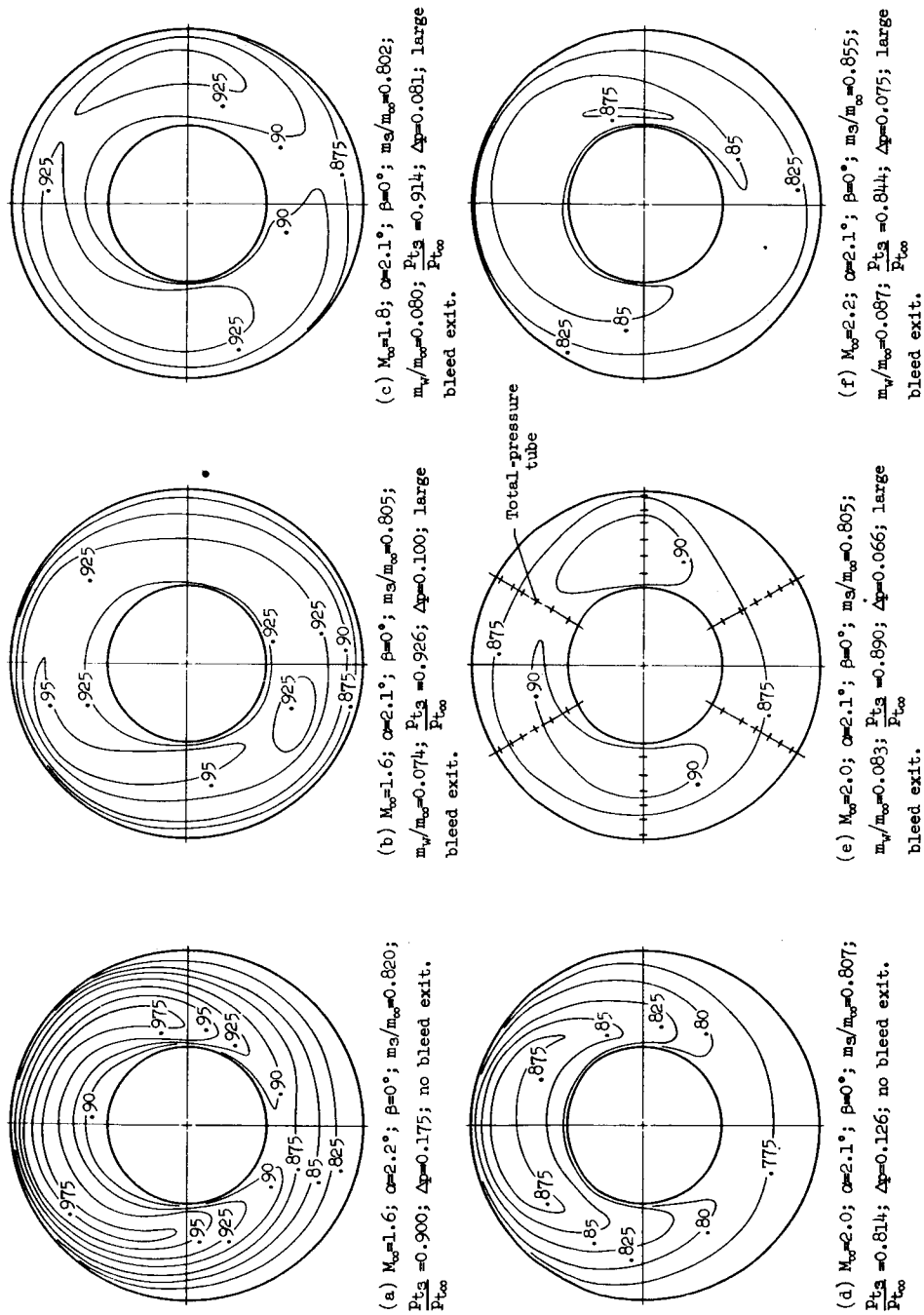


Figure 7.- Contours of local total-pressure recovery,  $\frac{(P_{t3})_{\text{local}}}{P_{t\infty}}$ , at the compressor face for no bleed ( $P_{5E_0}$ ) and bleed ( $P_{15E_1}$ ) configurations.

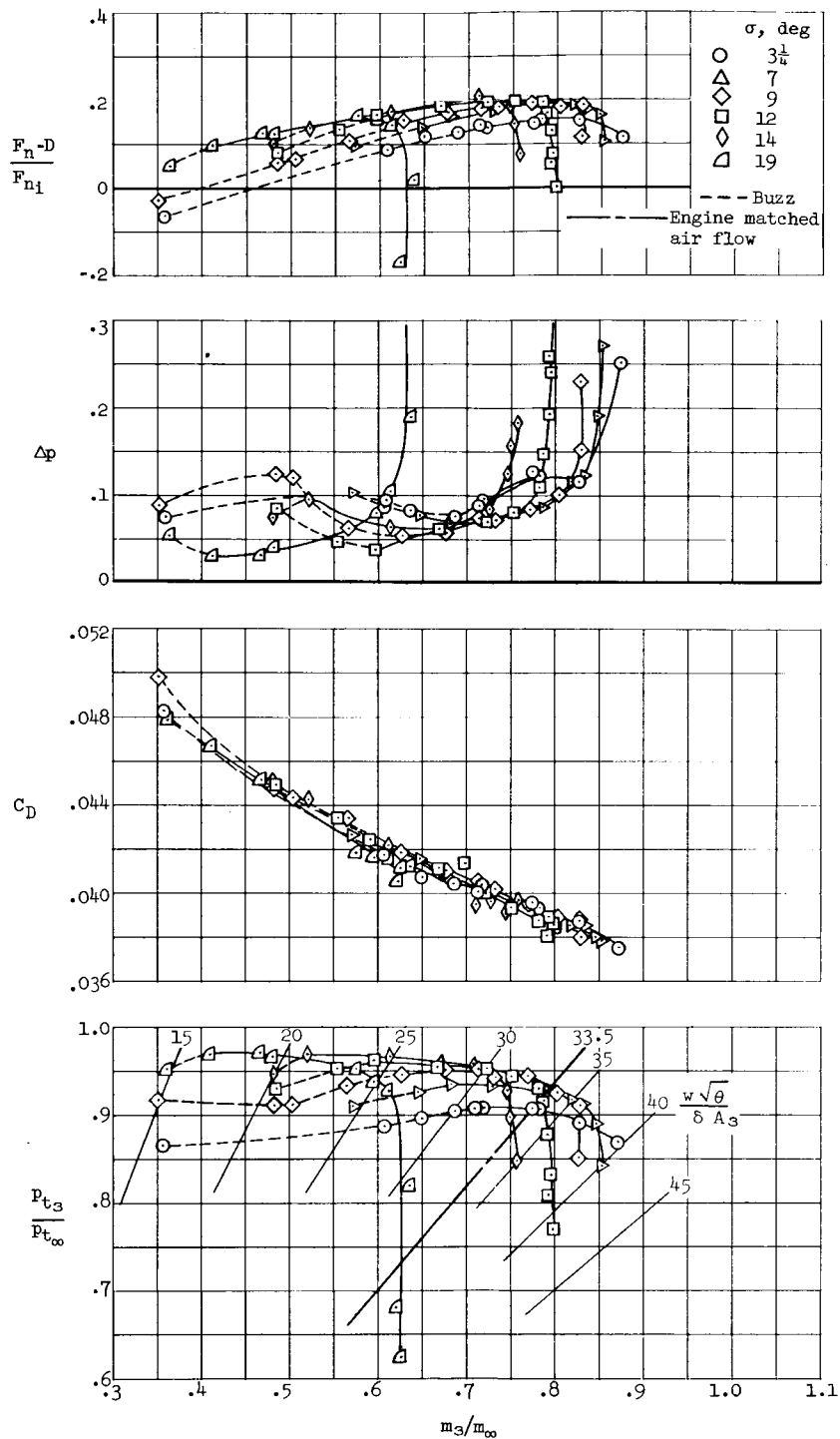
(a)  $M_\infty=1.6$ 

Figure 8.- Inlet performance with various variable-wedge half-angles;  
 $\alpha=2^\circ$ ,  $P_{15}E_l$  configuration.

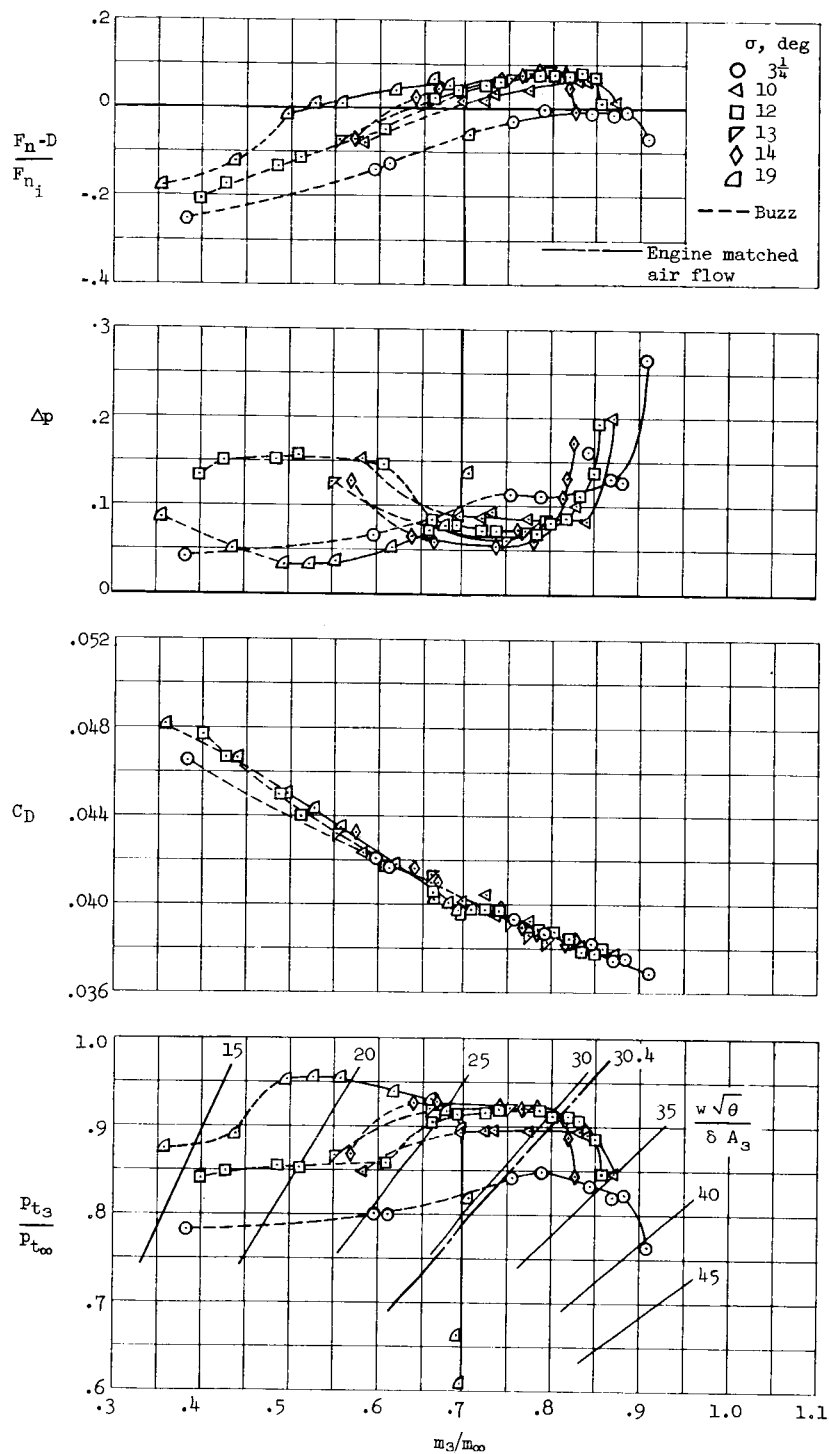
(b)  $M_\infty=1.8$ 

Figure 8.- Continued.



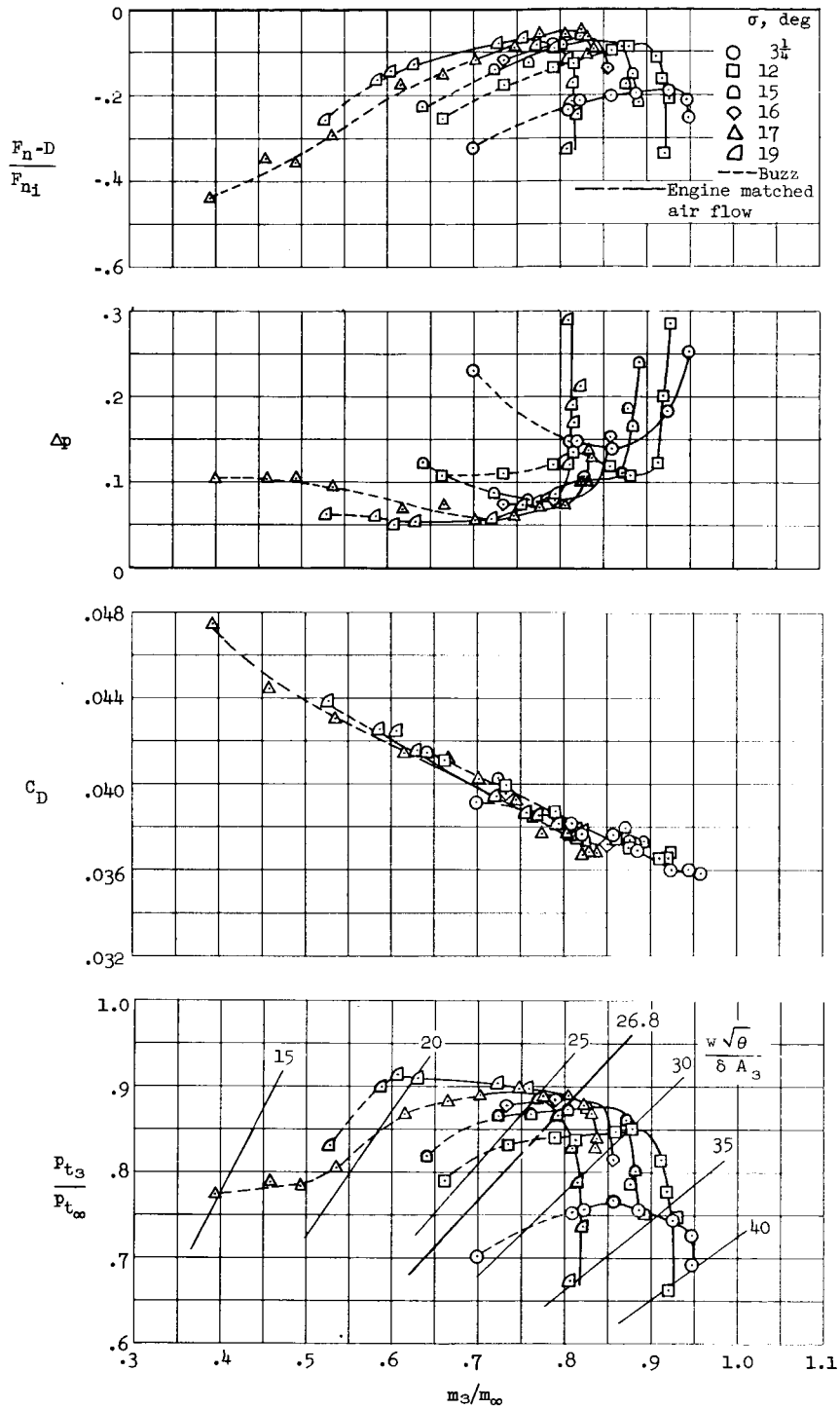
(c)  $M_\infty=2.0$ 

Figure 8.- Continued.

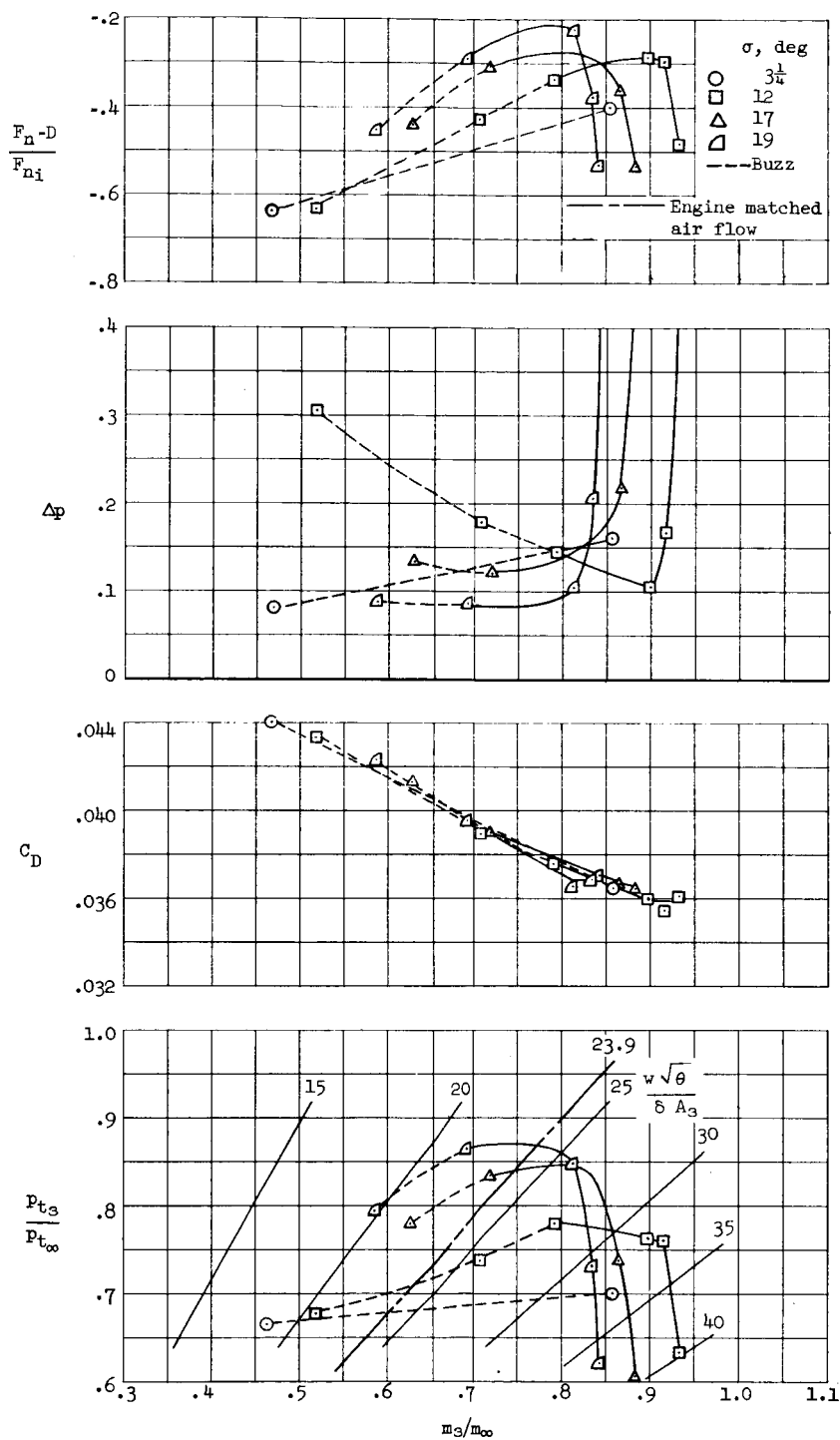
(d)  $M_\infty=2.1$ 

Figure 8.- Continued.

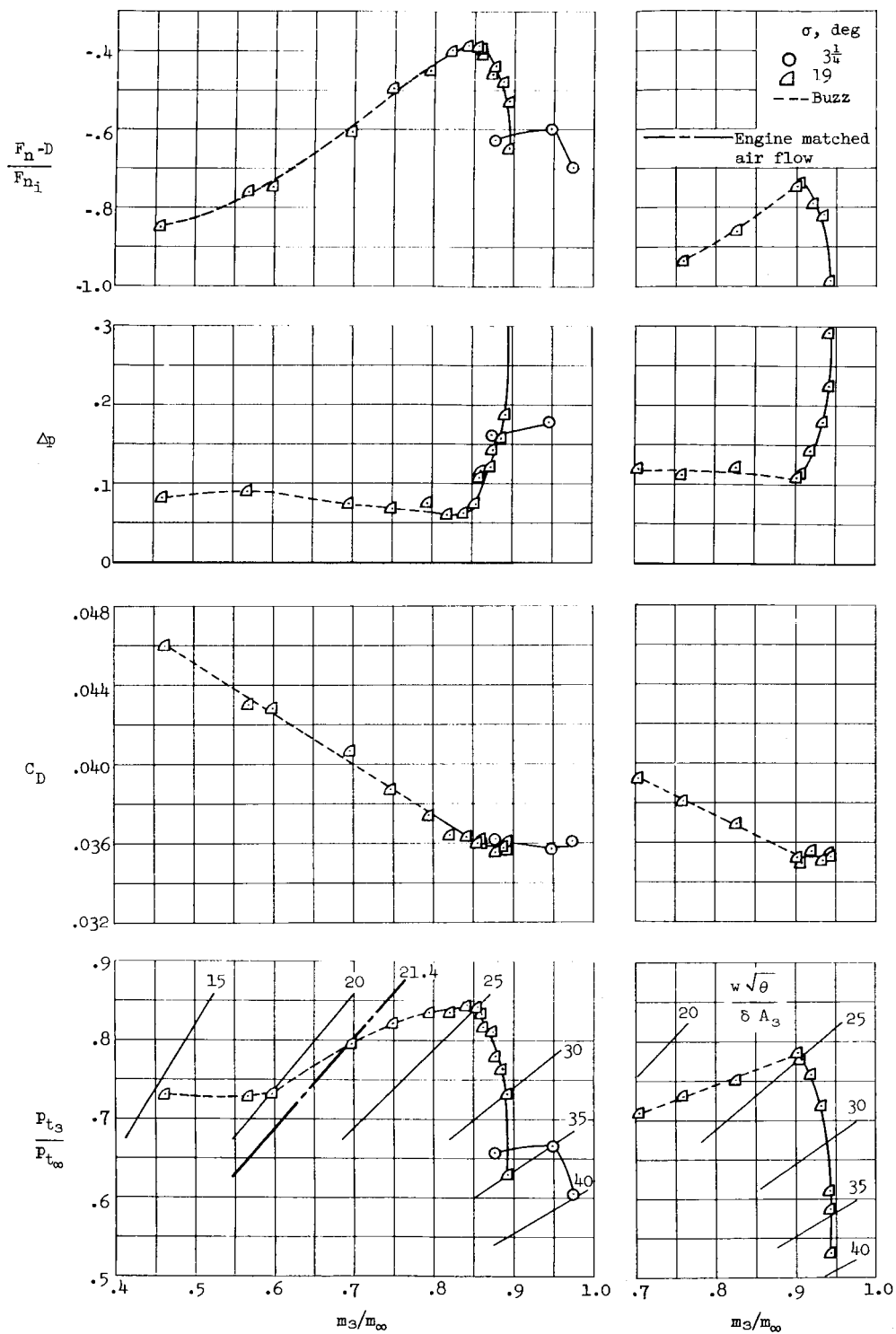
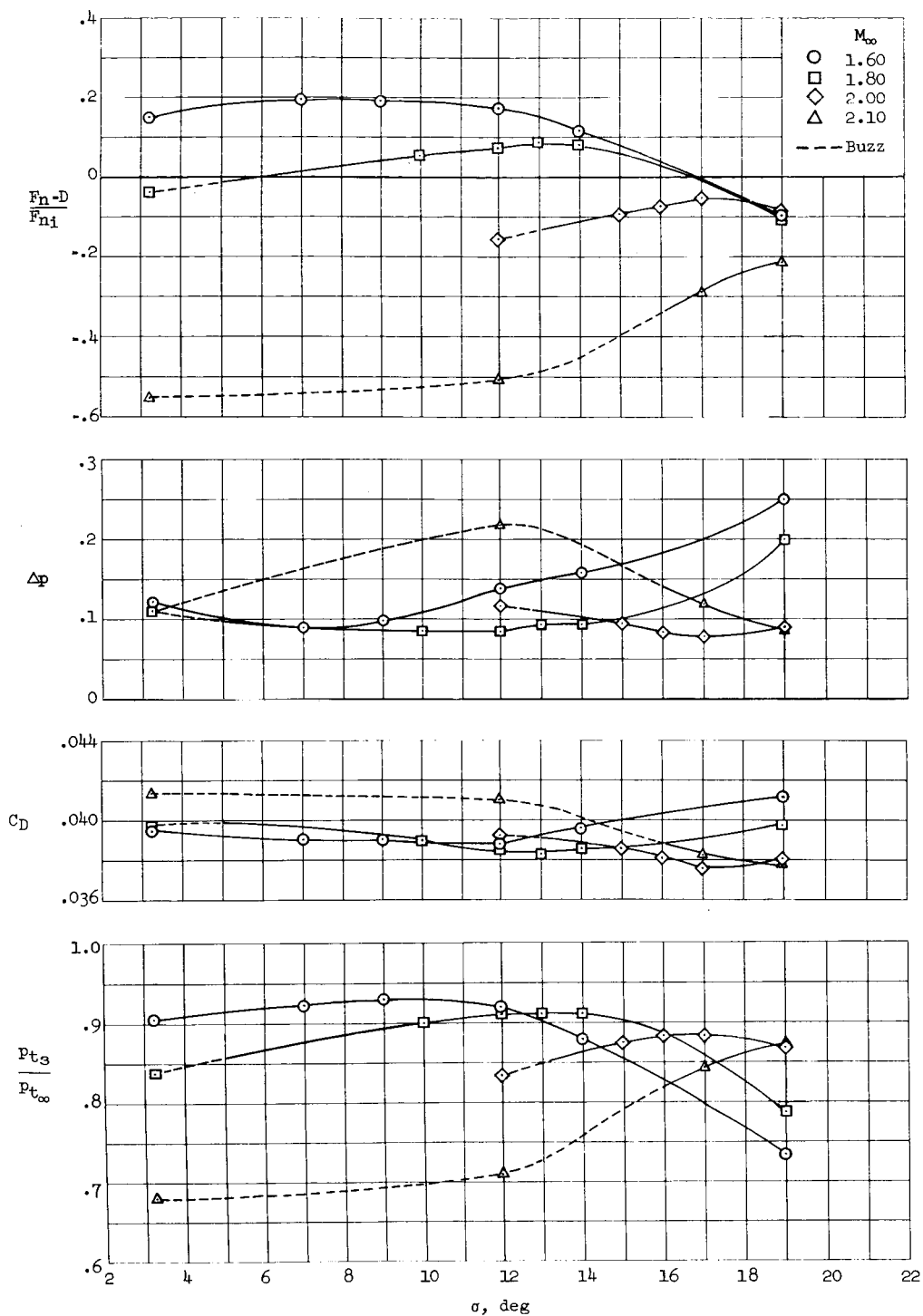
(e)  $M_\infty=2.2$ (f)  $M_\infty=2.35$ 

Figure 8.- Concluded.



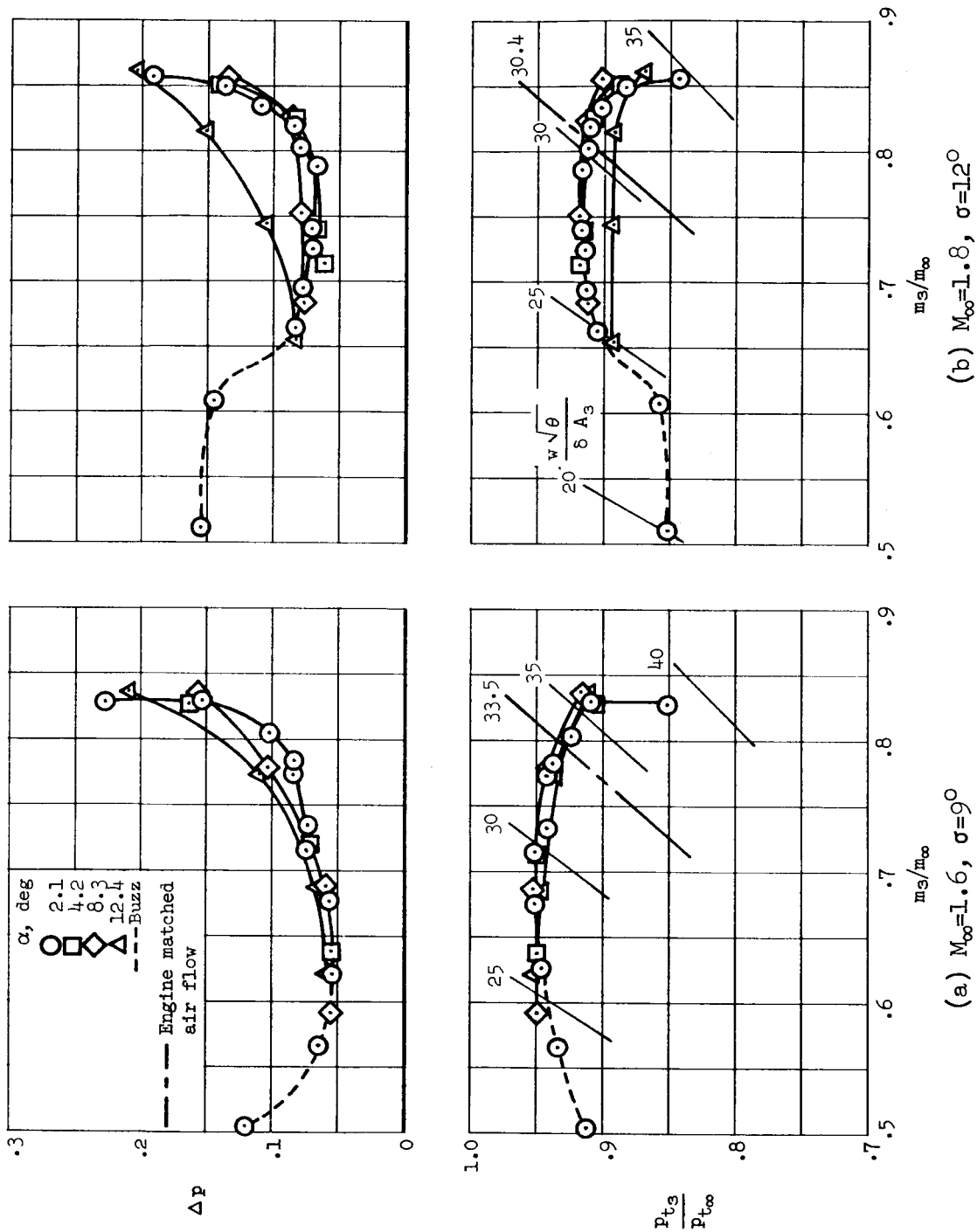


Figure 10.- Performance of P15E1 configuration at various angles of attack.

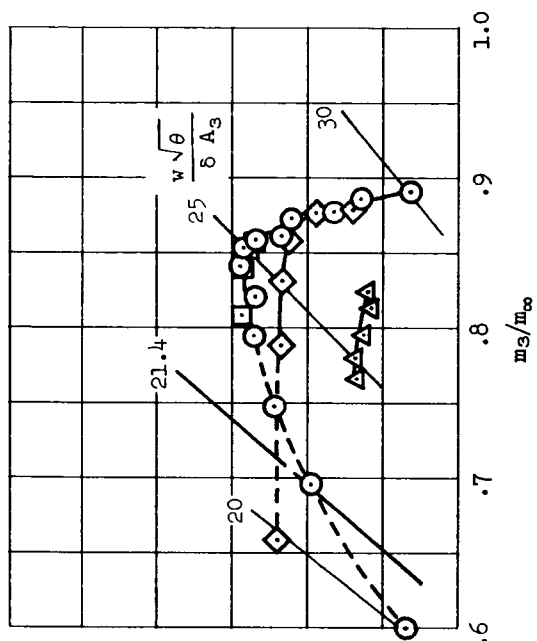
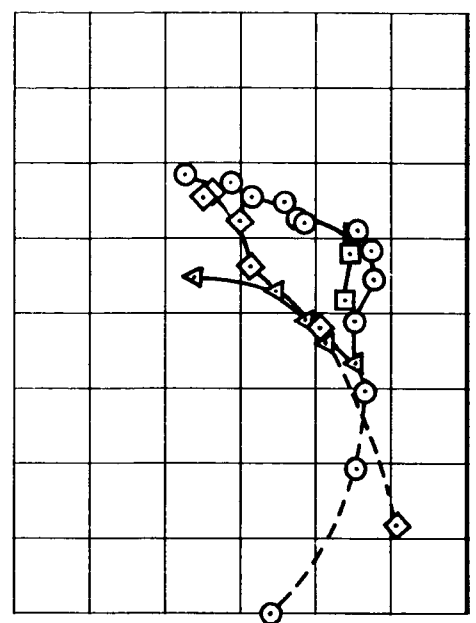
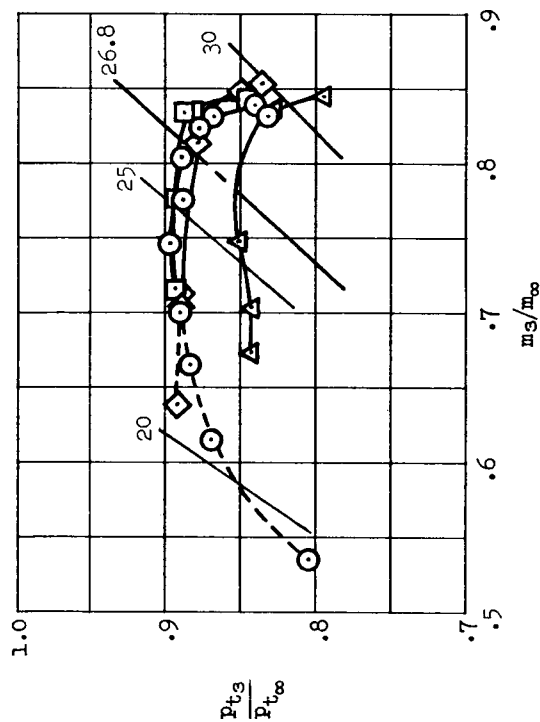
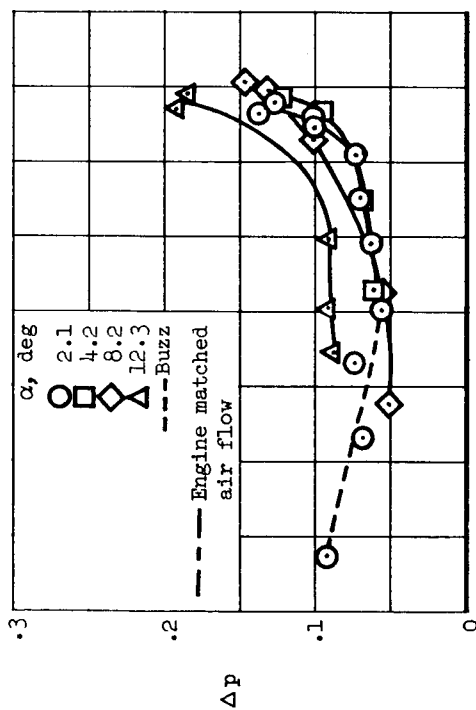
(d)  $M_\infty=2.2$ ,  $\sigma=19^\circ$ 

Figure 10.- Concluded.

(c)  $M_\infty=2.0$ ,  $\sigma=17^\circ$

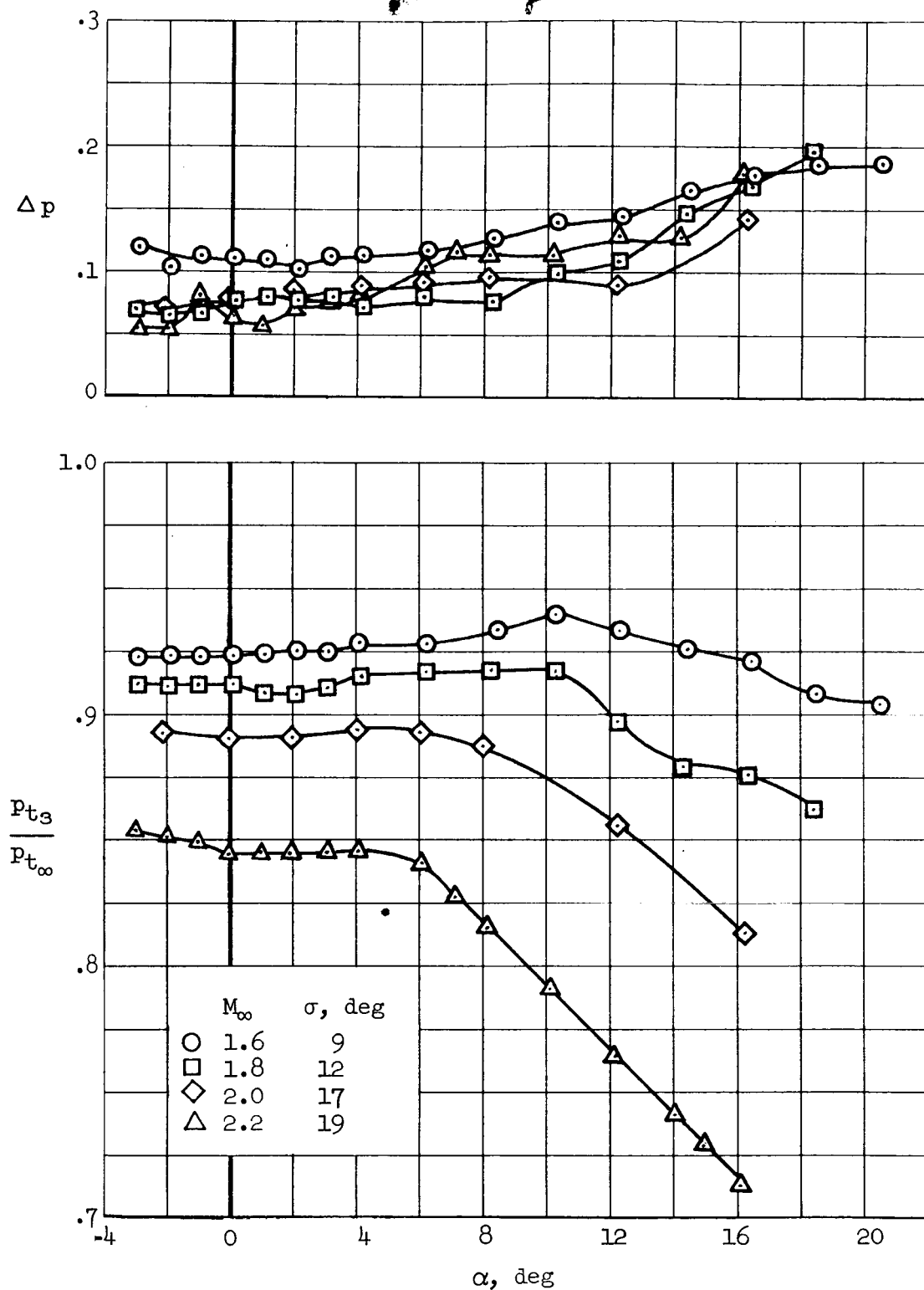


Figure 11.- Angle-of-attack characteristics of  $P_{15}E_7$  configuration near matched mass flow.

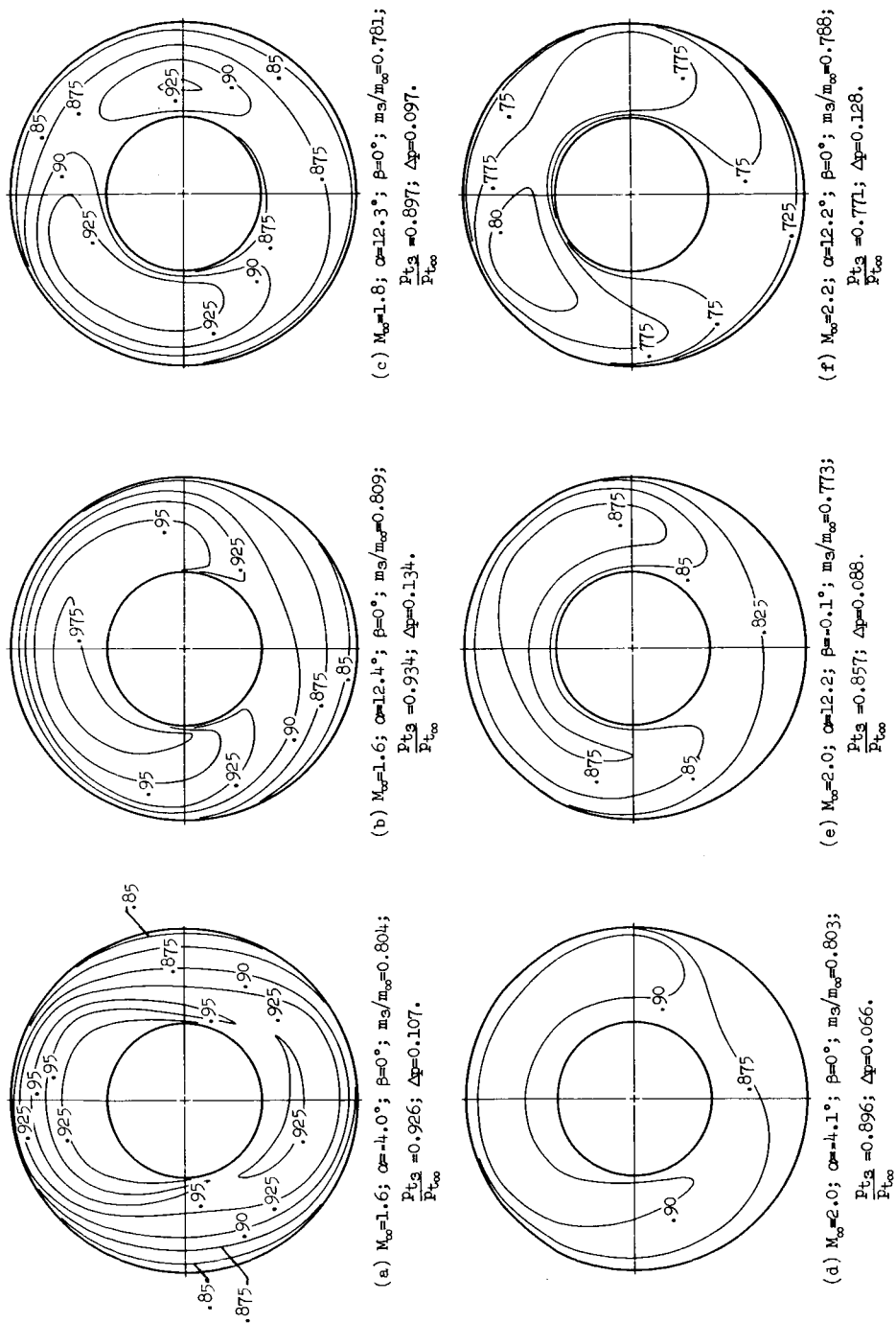


Figure 12.- Contours of local total-pressure recovery,  $\frac{(p_{t3})_{\text{local}}}{p_{t\infty}}$ , at the compressor face for  $P_{15}E_1$  configuration at angles of attack and near engine matched mass flow.



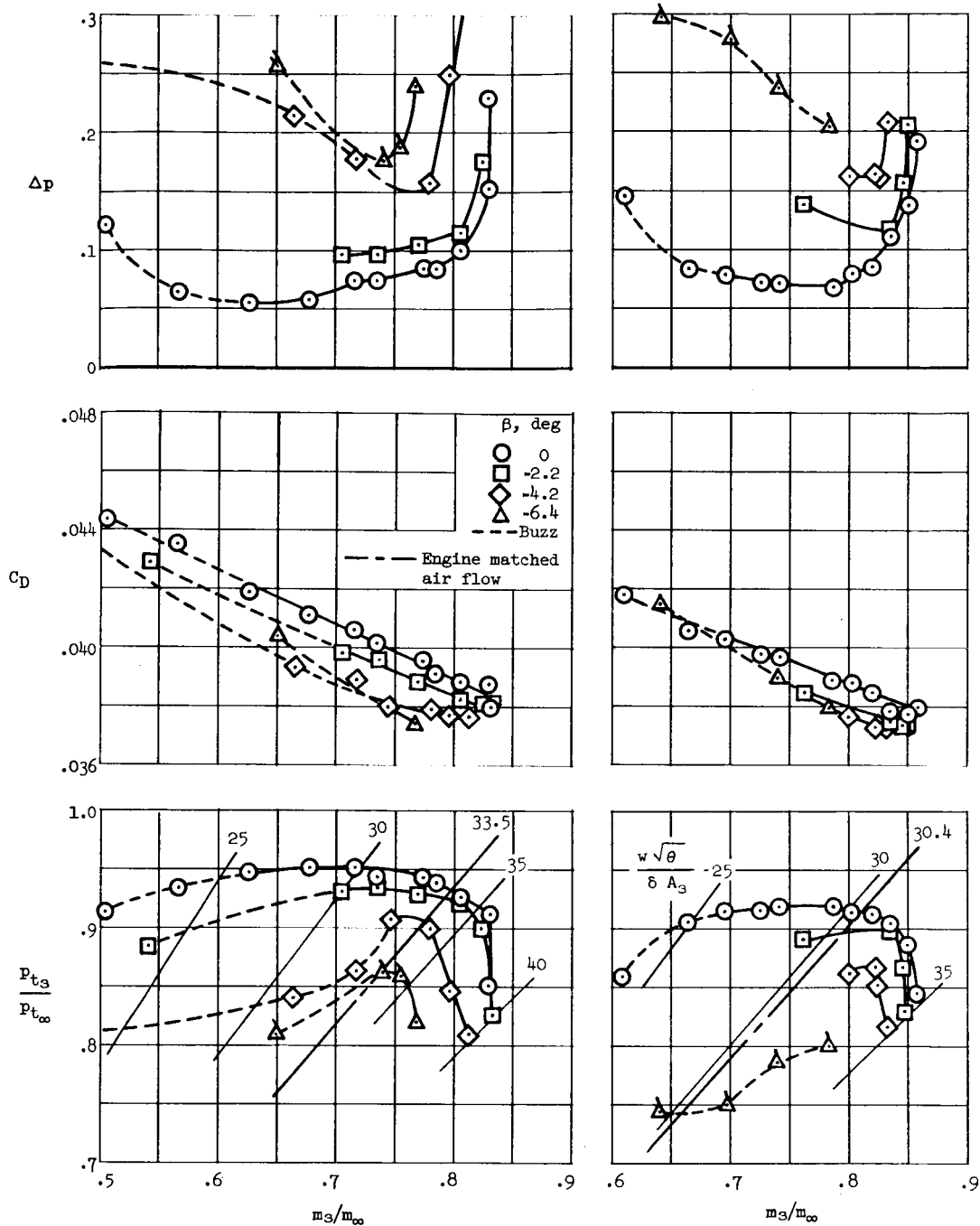
(a)  $M_\infty=1.6$ ,  $\sigma=9^\circ$ (b)  $M_\infty=1.8$ ,  $\sigma=12^\circ$ 

Figure 13.- Effect of sideslip angle on performance of  $P_{15}E_1$  configuration with symmetric wedge angles; angle of attack of  $2^\circ$  except where flagged symbols indicate  $\alpha=0^\circ$ .

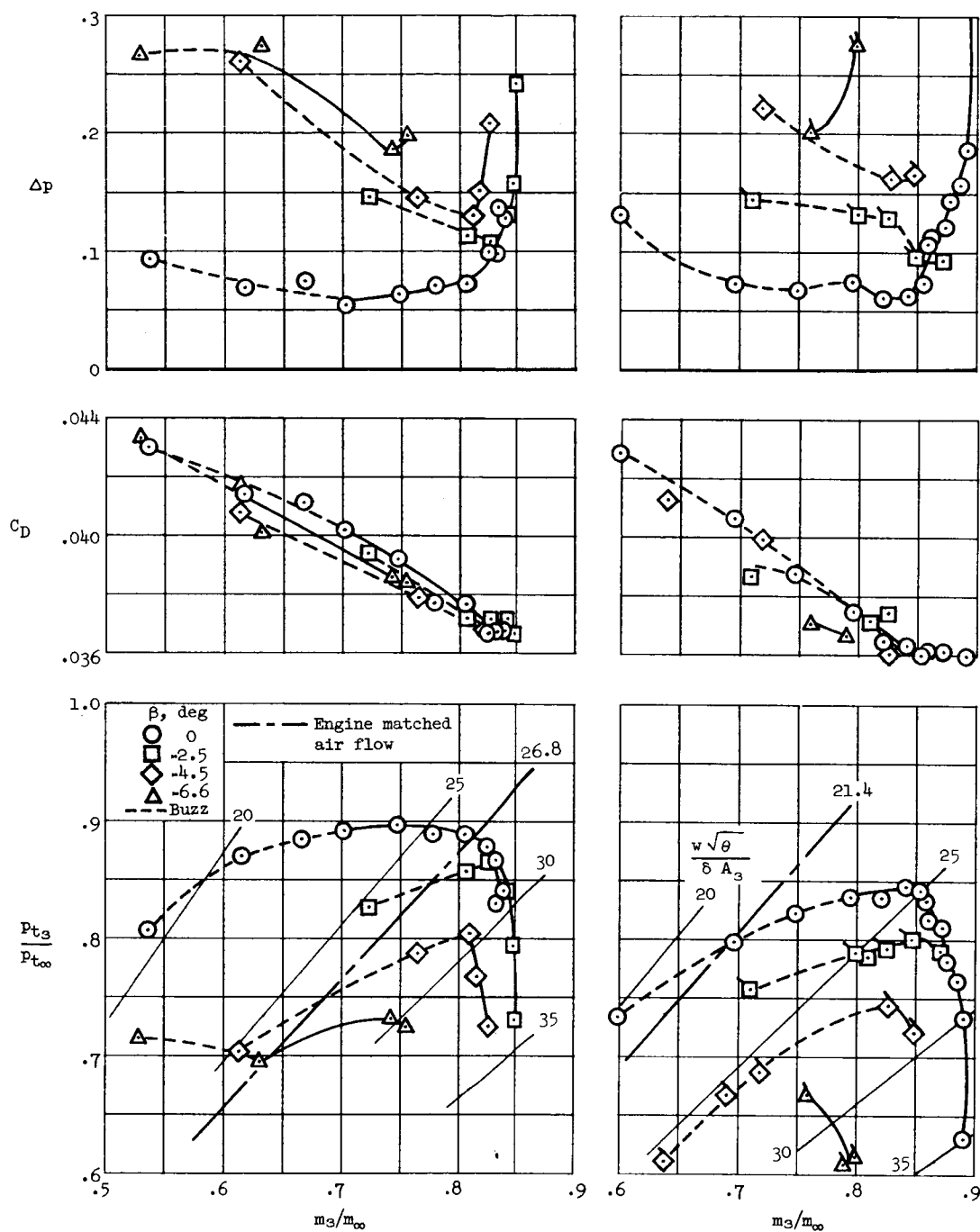
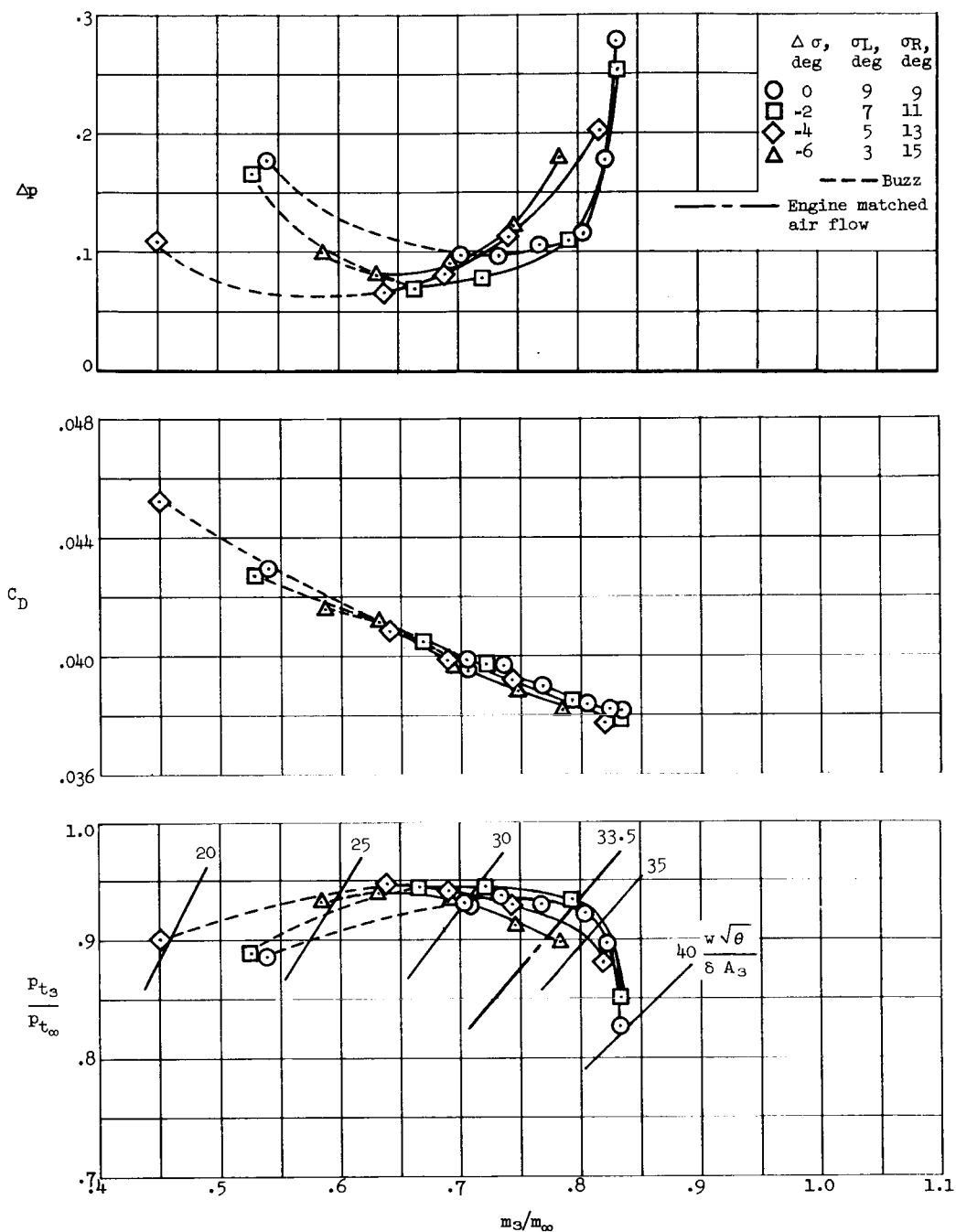
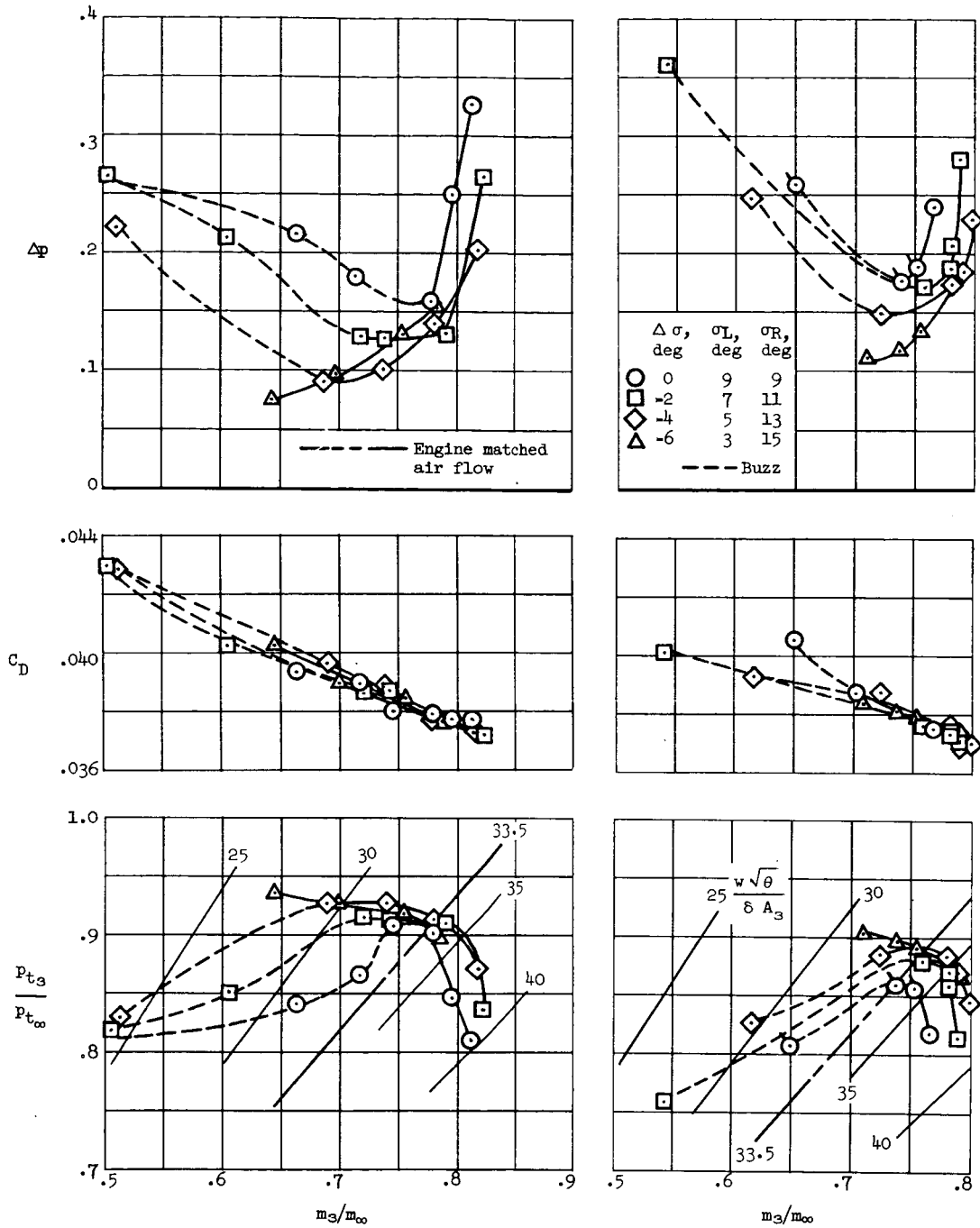
(c)  $M_\infty=2.0, \sigma=17^\circ$ (d)  $M_\infty=2.2, \sigma=19^\circ$ 

Figure 13.- Concluded.



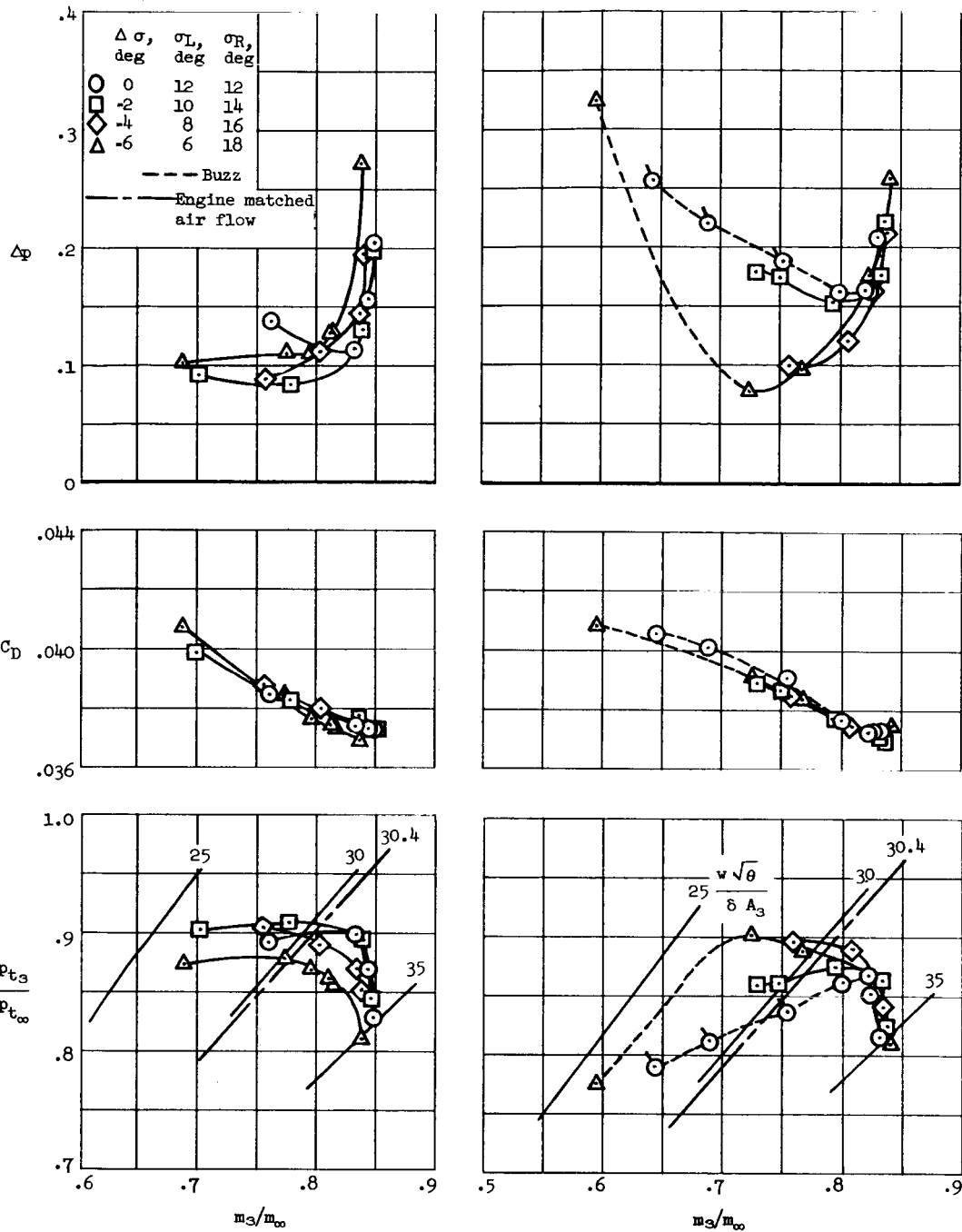
(a)  $M_\infty=1.6$ ;  $\beta=-2.2^\circ$ ;  $\frac{\sigma_L + \sigma_R}{2} = 9^\circ$

Figure 14.- Effect of asymmetric wedge deflection on inlet performance at angles of sideslip for  $P_{15}E_1$  configuration; angle of attack of  $2^\circ$  except where flagged symbols indicate  $\alpha=0^\circ$ .



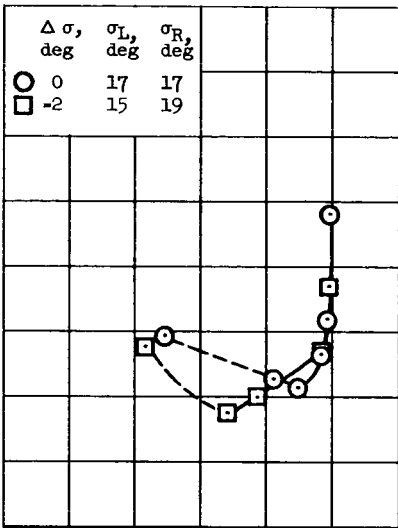
(b)  $M_\infty = 1.6$ ;  $\beta = -4.2^\circ$ ;  $\frac{\sigma_L + \sigma_R}{2} = 9^\circ$       (c)  $M_\infty = 1.6$ ;  $\beta = -6.2^\circ$ ;  $\frac{\sigma_L + \sigma_R}{2} = 9^\circ$

Figure 14.- Continued.

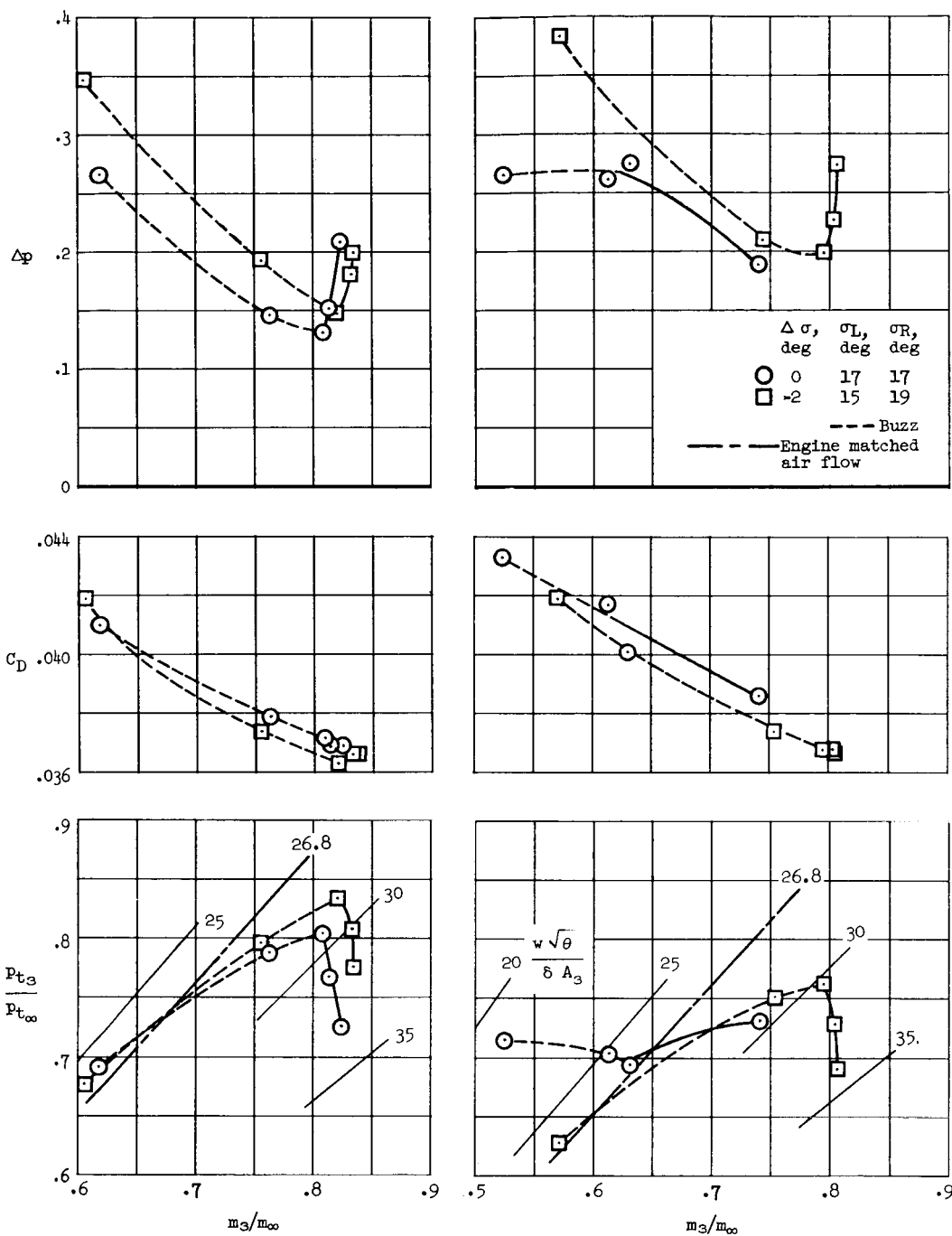


(d)  $M_\infty=1.8; \beta=-2.3^\circ; \frac{\sigma_L + \sigma_R}{2}=12^\circ$  (e)  $M_\infty=1.8; \beta=-4.3^\circ; \frac{\sigma_L + \sigma_R}{2}=12^\circ$

Figure 14.- Continued.



[REDACTED]



(h)  $M_\infty=2.0$ ;  $\beta=-4.5^\circ$ ;  $\frac{\sigma_L + \sigma_R}{2} = 17^\circ$

(i)  $M_\infty=2.0$ ;  $\beta=-6.5^\circ$ ;  $\frac{\sigma_L + \sigma_R}{2} = 17^\circ$

Figure 14.- Concluded.

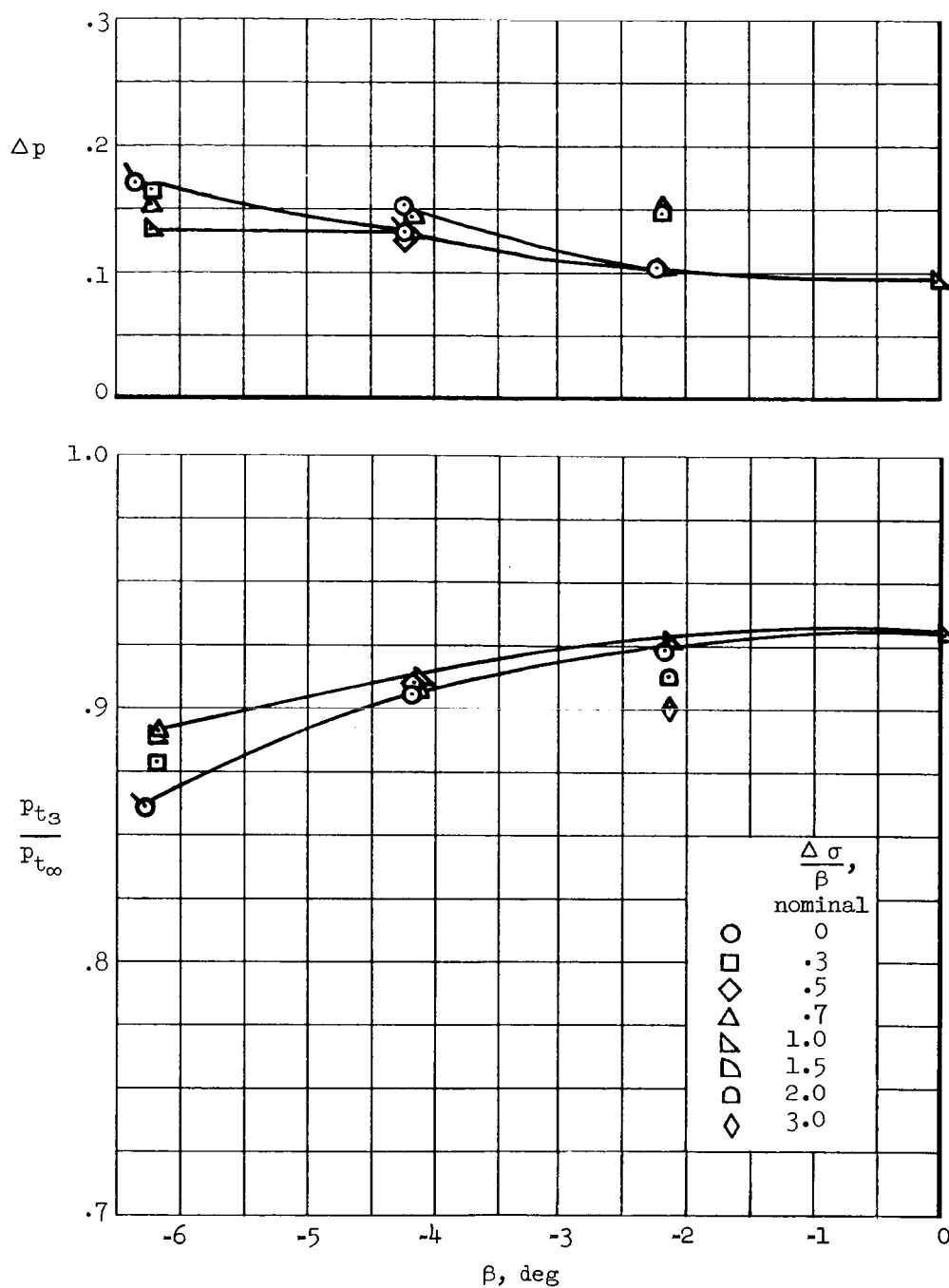
(a)  $M_\infty=1.6$ 

Figure 15.- Matched mass-flow performance of asymmetric and symmetric wedge inlets at angles of sideslip;  $P_{15}E_1$  configuration at  $\alpha=2^\circ$  except where flagged symbols indicate  $\alpha=0^\circ$ .



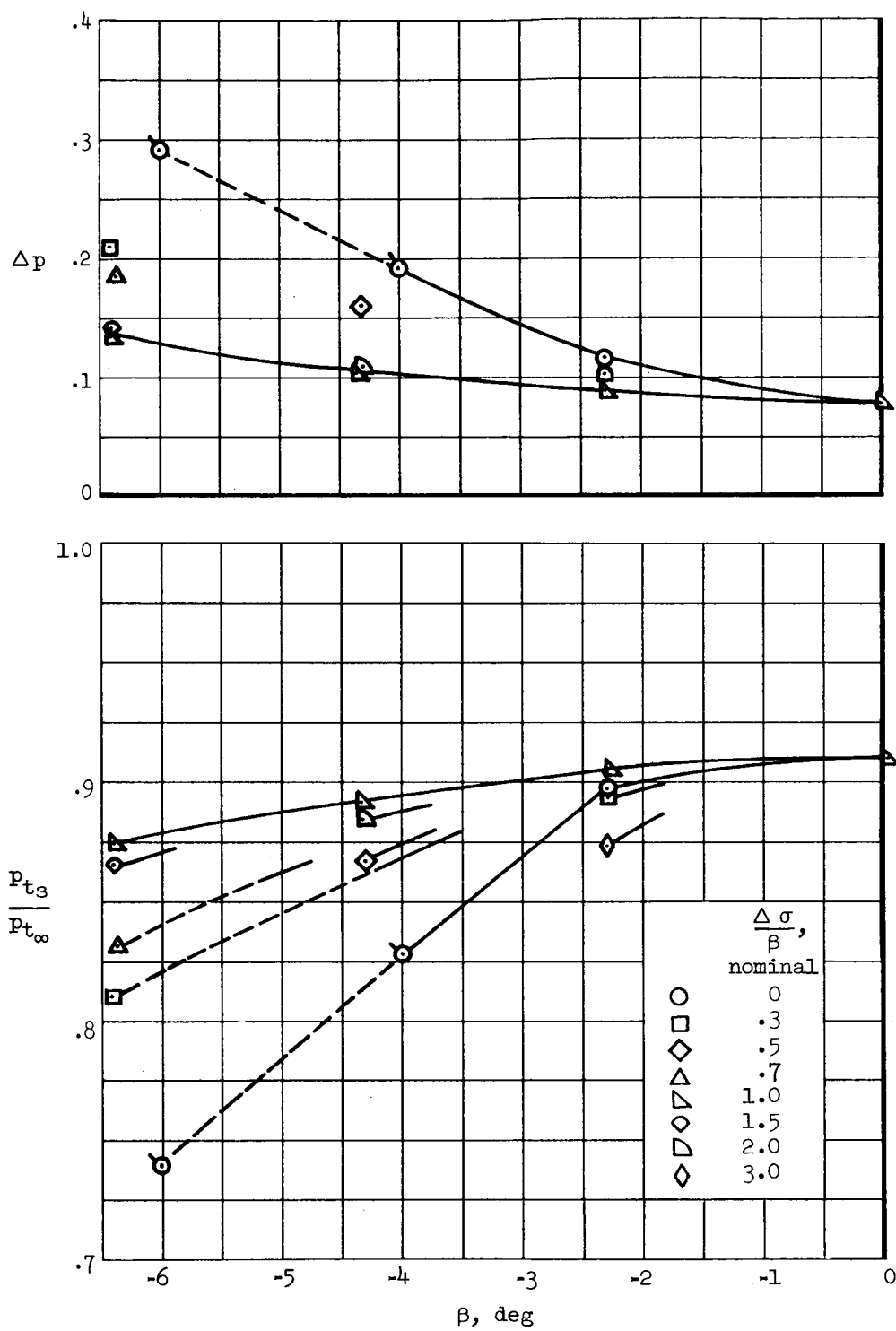
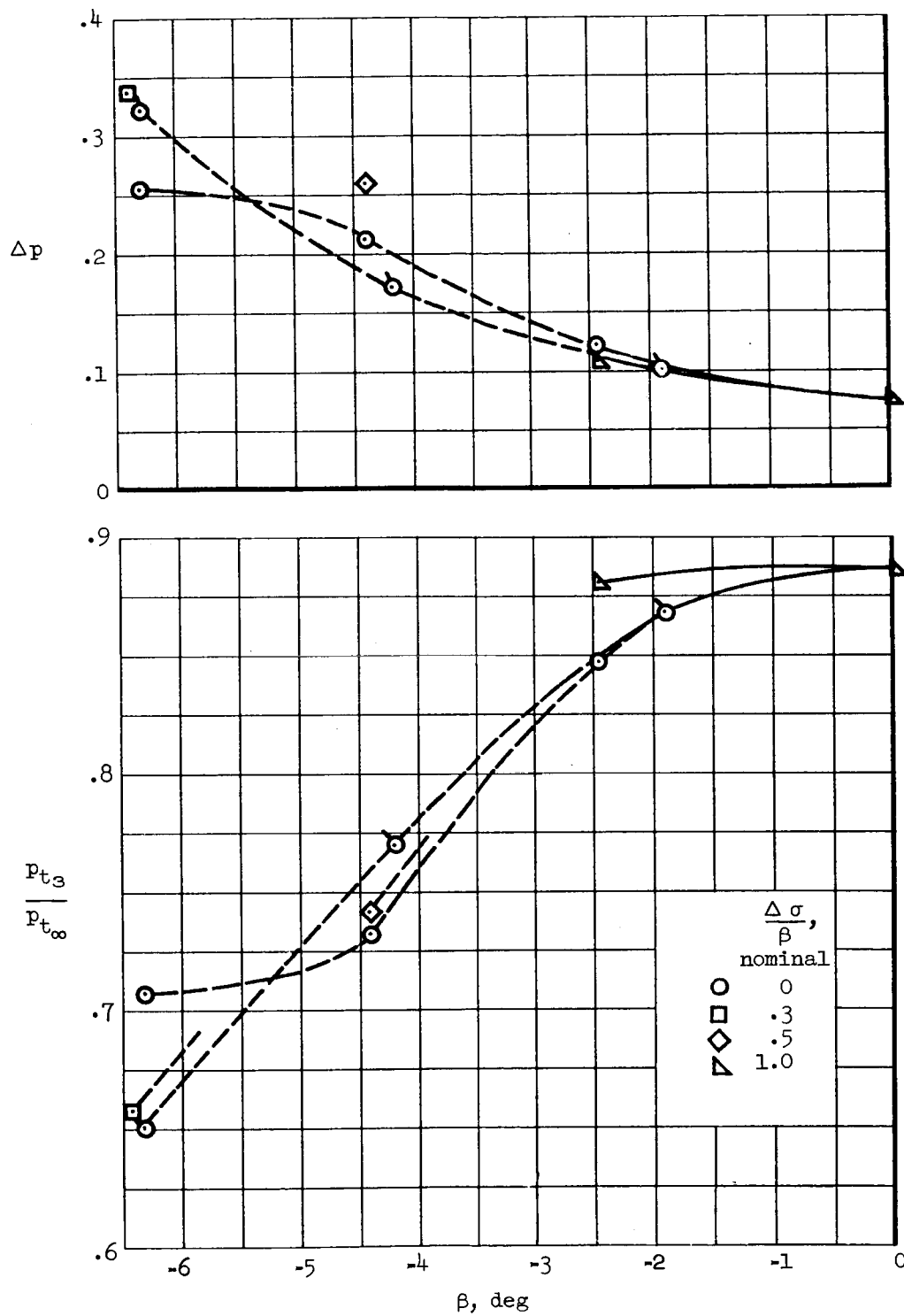
(b)  $M_{\infty}=1.8$ 

Figure 15.- Continued.

A-141



(c)  $M_\infty=2.0$

Figure 15.- Concluded.

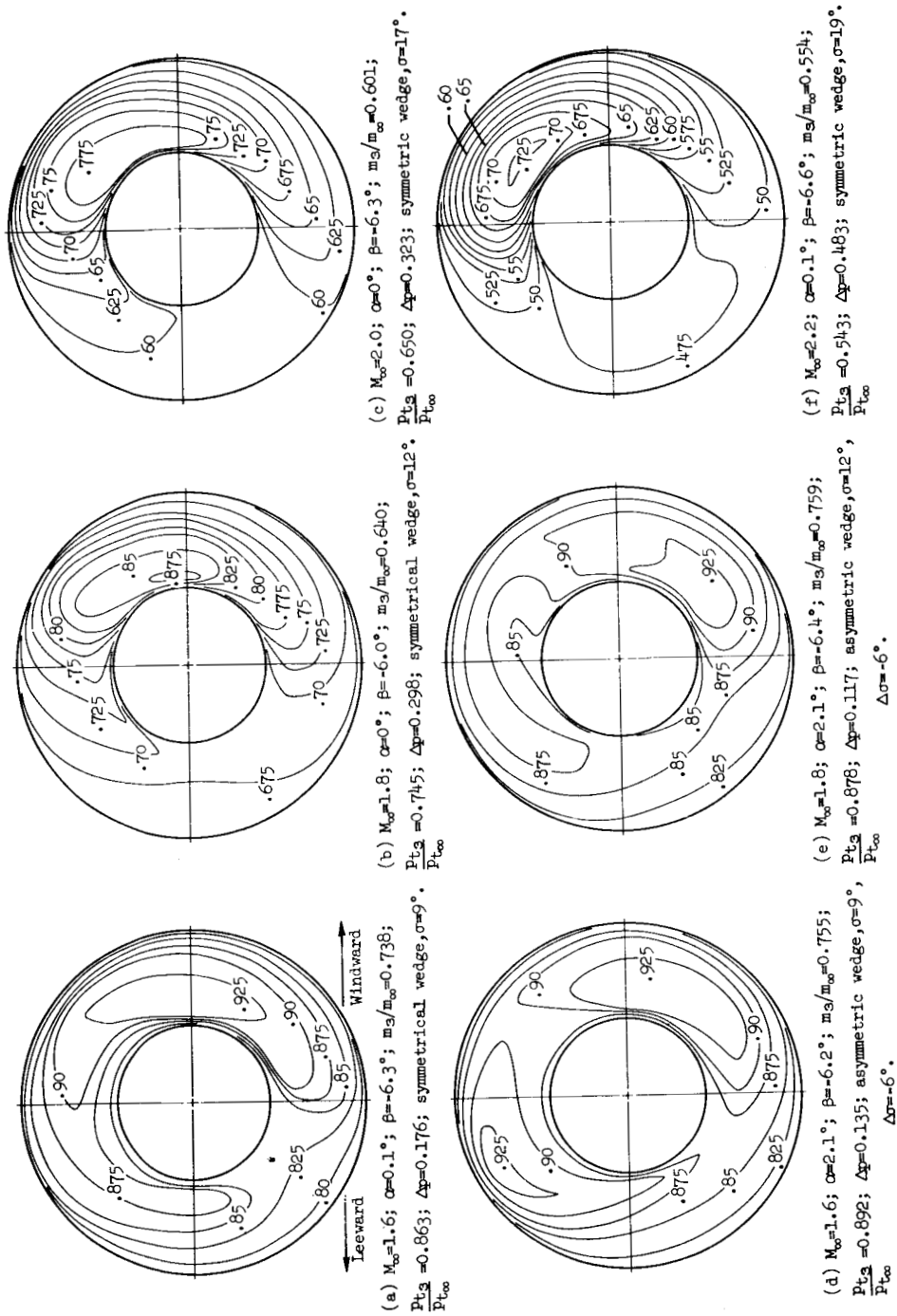
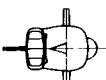

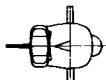

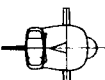

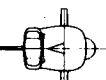



Figure 16.- Contours of local total-pressure recovery,  $\frac{(P_{t3})_{\text{local}}}{P_{t\infty}}$ , at the compressor face for symmetrical and asymmetrical wedge deflection at angles of sideslip;  $P_{15E_1}$  configuration at near engine matched mass flow.

NOTES: (1) Reynolds number is based on the diameter of a circle with the same area as that of the capture area of the inlet.

(2) The symbol \* denotes the occurrence of buzz.

Report and facility	Description		Test parameters					Test data			Performance		Remarks		
			Free-stream Mach number	Reynolds number $\times 10^{-5}$	Angle of attack, deg	Angle of yaw, deg	Drag	Inlet-flow profile	Discharge-flow profile	Maximum total-pressure recovery	Mass-flow ratio				
NASA MEMO 2-2-59A Ames 9- by 7-Foot Wind Tunnel			2	Porous surface	2.0	.64	2.1	0	✓		✓		0.89	0.39 - .84*	Asymmetric wedge deflection
				Porous surface	2.0	.64	12.3	0		✓	✓		.86	.67 - .84*	
				Porous surface	1.8	.64	2.1	-6.4	✓		✓		.88	.60 - .82*	
NASA MEMO 2-2-59A Ames 9- by 7-Foot Wind Tunnel			2	Porous surface	2.0	.64	2.1	0	✓		✓		0.89	0.39 - .84*	Asymmetric wedge deflection
				Porous surface	2.0	.64	12.3	0		✓	✓		.86	.67 - .84*	
				Porous surface	1.8	.64	2.1	-6.4	✓		✓		.88	.60 - .82*	
NASA MEMO 2-2-59A Ames 9- by 7-Foot Wind Tunnel			2	Porous surface	2.0	.64	2.1	0	✓		✓		0.89	0.39 - .84*	Asymmetric wedge deflection
				Porous surface	2.0	.64	12.3	0		✓	✓		.86	.67 - .84*	
				Porous surface	1.8	.64	2.1	-6.4	✓		✓		.88	.60 - .82*	
NASA MEMO 2-2-59A Ames 9- by 7-Foot Wind Tunnel			2	Porous surface	2.0	.64	2.1	0	✓		✓		0.89	0.39 - .84*	Asymmetric wedge deflection
				Porous surface	2.0	.64	12.3	0		✓	✓		.86	.67 - .84*	
				Porous surface	1.8	.64	2.1	-6.4	✓		✓		.88	.60 - .82*	

#### Bibliography

These strips are provided for the convenience of the reader and can be removed from this report to compile a bibliography of NACA inlet reports. This page is being added only to inlet reports and is on a trial basis.